

PREPARATION AND OPERATIONS OF THE MISSION PERFORMANCE
CENTRE (MPC) FOR THE COPERNICUS SENTINEL-3 MISSION

S3-A OLCI Cyclic Performance Report

Cycle No. 018

Start date: 18/05/2017

End date: 14/06/2017



*Mission
Performance
Centre*



Ref.: S3MPC.ACR.PR.01-018

Issue: 1.1

Date: 22/06/2017

Contract: 4000111836/14/I-LG

Customer: ESA	Document Ref.: S3MPC.ACR.PR.01-018
Contract No.: 4000111836/14/I-LG	Date: 22/06/2017
	Issue: 1.1

Project:	PREPARATION AND OPERATIONS OF THE MISSION PERFORMANCE CENTRE (MPC) FOR THE COPERNICUS SENTINEL-3 MISSION		
Title:	S3-A OLCI Cyclic Performance Report		
Author(s):	OLCI ESLs		
Approved by:	L. Bourg, OLCI ESL Coordinator	Authorized by	Frédéric Rouffi, OPT Technical Performance Manager
Distribution:	ESA, EUMETSAT, S3MPC consortium		
Accepted by ESA	S. Dransfeld, MPC Deputy TO for OPT P. Féménias, MPC TO		
Filename	S3MPC.ACR.PR.01-018 - i1r1 - OLCI Cyclic Report 018.docx		

Disclaimer

The work performed in the frame of this contract is carried out with funding by the European Union. The views expressed herein can in no way be taken to reflect the official opinion of either the European Union or the European Space Agency.





Sentinel-3 MPC
S3-A OLCI Cyclic Performance Report
Cycle No. 018

Ref.: S3MPC.ACR.PR.01-018
 Issue: 1.1
 Date: 22/06/2017
 Page: iii

Changes Log

Version	Date	Changes
1.0	20/06/2017	First Version
1.1	22/06/2017	Correction of broken internal links (to Figures). Inclusion of Land Products validation material.

List of Changes

Version	Section	Answers to RID	Changes
1.1	3		Update with land validation inputs



Sentinel-3 MPC
S3-A OLCI Cyclic Performance Report
Cycle No. 018

Ref.: S3MPC.ACR.PR.01-018
 Issue: 1.1
 Date: 22/06/2017
 Page: iv

Table of content

TABLE OF CONTENT	IV
LIST OF FIGURES	VI
1 INSTRUMENT MONITORING	1
1.1 CCD TEMPERATURES.....	1
1.2 RADIOMETRIC CALIBRATION	2
1.2.1 <i>Dark Offsets [OLCI-L1B-CV-230]</i>	4
1.2.2 <i>Instrument response and degradation modelling [OLCI-L1B-CV-250]</i>	7
1.2.3 <i>Ageing of nominal diffuser [OLCI-L1B-CV-240]</i>	14
1.2.4 <i>Updating of calibration ADF [OLCI-L1B-CV-260]</i>	18
1.2.5 <i>Radiometric Calibrations for sun azimuth angle dependency and Yaw Manoeuvres for Solar Diffuser on-orbit re-characterization [OLCI-L1B-CV-270 and OLCI-L1B-CV-280]</i>	18
1.3 SPECTRAL CALIBRATION [OLCI-L1B-CV-400].....	18
1.4 SIGNAL TO NOISE ASSESSMENT [OLCI-L1B-CV-620]	21
1.4.1 <i>SNR from Radiometric calibration data</i>	21
1.4.2 <i>SNR from EO data</i>	23
1.5 GEOMETRIC CALIBRATION/VALIDATION	23
2 OLCI LEVEL 1 PRODUCT VALIDATION	25
2.1 [OLCI-L1B-CV-300], [OLCI-L1B-CV-310] – RADIOMETRIC VALIDATION	25
2.1.1 <i>S3ETRAC Service</i>	25
2.1.2 <i>Radiometric validation with DIMITRI</i>	26
2.1.3 <i>Radiometric validation with OSCAR</i>	29
3 LEVEL 2 LAND PRODUCTS VALIDATION	31
3.1 [OLCI-L2LRF-CV-300].....	31
3.1.1 <i>Indirect validation: Temporal evolution of OTCI over core validation sites</i>	31
3.1.2 <i>Direct validation: example from UKNfo site</i>	37
3.2 [OLCI-L2LRF-CV-410 & OLCI-L2LRF-CV-420] – CLOUD MASKING & SURFACE CLASSIFICATION FOR LAND PRODUCTS	39
3.3 VALIDATION OF INTEGRATED WATER VAPOUR OVER LAND	39
4 LEVEL 2 WATER PRODUCTS VALIDATION	40
4.1 [OLCI-L2-CV-210, OLCI-L2-CV-220] – VICARIOUS CALIBRATION OF THE NIR AND VIS BANDS.....	40
4.2 [OLCI-L2WLR-CV-300, OLCI-L2WLR-CV-310, OLCI-L2WLR-CV-32, OLCI-L2WLR-CV-330, OLCI-L2WLR-CV-340, OLCI-L2WLR-CV-350, OLCI-L2WLR-CV-360 AND OLCI-L2WLR-CV-370] – LEVEL 2 WATER-LEAVING REFLECTANCE PRODUCT VALIDATION.....	40
4.3 [OLCI-L2WLR-CV530] VALIDATION OF AEROSOL PRODUCT.....	45
5 LEVEL 2 SYN PRODUCTS VALIDATION	52
5.1 [SYN-L2-CV-100]	52
6 EVENTS	53
7 APPENDIX A	54



Sentinel-3 MPC

S3-A OLCI Cyclic Performance Report

Cycle No. 018

Ref.: S3MPC.ACR.PR.01-018

Issue: 1.1

Date: 22/06/2017

Page: v

	<p>Sentinel-3 MPC</p> <p>S3-A OLCI Cyclic Performance Report</p> <p>Cycle No. 018</p>	<p>Ref.: S3MPC.ACR.PR.01-018</p> <p>Issue: 1.1</p> <p>Date: 22/06/2017</p> <p>Page: vi</p>
--	--	--

List of Figures

Figure 1: long term monitoring of CCD temperatures using minimum value (top), time averaged values (middle), and maximum value (bottom) provided in the annotations of the Radiometric Calibration Level 1 products, for the Shutter frames, all radiometric calibrations so far. ----- 1

Figure 2: Same as Figure 1 for diffuser frames. ----- 2

Figure 3: Sun azimuth angles during acquired Radiometric Calibrations (diffuser frame) on top of nominal yearly cycle (black curve). Diffuser 1 with diamonds, diffuser 2 with crosses, 2016 acquisitions in blue, 2017 in red. ----- 3

Figure 4: Sun geometry during radiometric Calibrations on top of characterization ones (diffuser frame) 3

Figure 5: Dark Offset for band Oa1 (top) and Oa21 (bottom), all radiometric calibrations so far except the first one (orbit 183) for which the instrument was not thermally stable yet. ----- 4

Figure 6: map of periodic noise for the 5 cameras, for band Oa21. X-axis is detector number (East part, from 540 to 740, where the periodic noise occurs), Y-axis is the orbit number. The counts have been corrected from the west detectors mean value (not affected by periodic noise). Periodic noise amplitude is high in camera 2, 3 and 4. It is lower in camera 4 and small in camera 1. ----- 5

Figure 7: Dark Current for band Oa1 (top) and Oa21 (bottom), all radiometric calibrations so far except the first one (orbit 183) for which the instrument was not thermally stable yet. ----- 6

Figure 8: left column: ACT mean on 400 first detectors of Dark Current coefficients for spectral band Oa01 (top) and Oa21 (bottom). Right column: same as left column but for Standard deviation instead of mean. We see an increase of the DC level as a function of time especially for band Oa21. A possible explanation could be the increase of the number of hot pixels which is more important in Oa21 because this band is made of more CCD lines than band Oa01 and thus receives more cosmic rays impacts. It is known that cosmic rays degrade the structure of the CCD, generating more and more hot pixels at long term scales. ----- 6

Figure 9: Gain Coefficients for band Oa1 (top) and Oa21 (bottom), all diffuser 1 radiometric calibrations so far except the first one (orbit 183) for which the instrument was not thermally stable yet. ----- 7

Figure 10: camera averaged gain relative evolution with respect to “best geometry” calibration (22/11), as a function of elapsed time since launch; one curve for each band (see colour code on plots), one plot for each module. The star tracker anomaly fix (6/04/16) is represented by a vertical red dashed line. ---- 8

Figure 11: Camera-averaged instrument evolution since channel programming change (25/04/2016) and up to most recent calibration (28/05/2017) versus wavelength.----- 9

Figure 12: For the 5 cameras: Evolution model performance, as camera-average and standard deviation of ratio of Model over Data vs. wavelength, for each orbit of the test dataset, including 8 calibration in extrapolation, with a colour code for each calibration from blue (oldest) to red (most recent).-----10

Figure 13: model performance: ratio of model over data for all pixels (x axis) of all orbits (y axis), for channel Oa4. The outlying orbit #40 is that of 31/03/2017. -----11

	<p>Sentinel-3 MPC</p> <p>S3-A OLCI Cyclic Performance Report</p> <p>Cycle No. 018</p>	<p>Ref.: S3MPC.ACR.PR.01-018</p> <p>Issue: 1.1</p> <p>Date: 22/06/2017</p> <p>Page: vii</p>
--	--	---

Figure 14: Evolution model performance, as ratio of Model over Data vs. pixels, all cameras side by side, over the whole current calibration dataset (since instrument programming update), including 8 calibration in extrapolation, channels Oa1 to Oa6. -----12

Figure 15: same as Figure 14 for channels Oa7 to Oa14. -----13

Figure 16: same as Figure 14 for channels Oa15 to Oa21.-----14

Figure 17: diffuser 1 ageing for spectral band Oa01. We see strong ACT low frequency structures that are due to residual of BRDF modelling. -----15

Figure 18: same as Figure 17 for spectral band Oa16. We use this band in order to normalize other bands and remove the ACT structures due to residual of BRDF modelling. Normalized curve for spectral band Oa01 is presented in Figure 19. -----16

Figure 19: same as Figure 17 after normalization by band Oa16. Ageing of the diffuser 1 is now visible in the 5 cameras.-----16

Figure 20: Diffuser 1 ageing as a function of wavelength (or spectral band). Ageing is visible in spectral band #1 to #5. -----17

Figure 21: Camera averaged ageing (normalized by band Oa16) as a function of time. Linear fit for each camera is plotted. The slope (% loss per year) and the correlation coefficient of the linear fits are written in the legend at the bottom.-----18

Figure 22: across track spectral calibration for all S02/S03 sequences since the beginning of the mission. Top plot is spectral line 1, middle plot is spectral line 2 and bottom plot spectral line 3.-----19

Figure 23: camera averaged spectral calibration as a function of orbit number (all spectral S02/S03 calibrations since the beginning of the mission are included). Top plot is spectral line 1, middle plot is spectral line 2 and bottom plot spectral line 3. -----20

Figure 24: spectral calibration as a function of time derived from all S09 sequences. From left to right column: the 5 cameras. From top to bottom: Used absorption line: 485 nm, 656 nm, 770 nm and 854 nm. -----20

Figure 25: Signal to Noise ratio as a function of the spectral band for the 5 cameras. These results have been computed from radiometric calibration data. All calibrations except first one (orbit 183) are presents with the colours corresponding to the orbit number (see legend). The SNR is very stable with time: the curves for all orbits are almost superimposed. The dashed curve is the ESA requirement. -----22

Figure 26: long-term stability of the SNR estimates from Calibration data, example of channel Oa1.-----23

Figure 27: histograms of geolocation errors for the along-track (left) and across-track (right) directions.24

Figure 28: georeferencing error in along-track (left) and across-track (right) directions for all the GCPs. 24

Figure 29: summary of S3ETRAC products generation for OLCI (number of OLCI L1 products Ingested, yellow – number of S3ETRAC extracted products generated, blue – number of S3ETRAC runs without generation of output product (data not meeting selection requirements), green – number of runs ending in error, red, one plot per site type). -----26

Figure 30: Time-series of the elementary ratios (observed/simulated) signal from S3A/OLCI for (top) band Oa8 and (bottom) band Oa17 over Six PICS Cal/Val sites. Dashed-green and orange lines indicate the 2% and 5% respectively. Error bars indicate the desert methodology uncertainty. -----27

Figure 31: The estimated gain values for S3A/OLCI over the 6 PICS sites identified by CEOS over the period September 2016 – June 2017 as a function of wavelength. Dashed-green and orange lines indicate the 2% and 5% respectively. Error bars indicate the desert methodology uncertainty. -----28

Figure 32: Time-series of the elementary ratios (observed/simulated) signal from (black)S2A/MSI and (blue) S3A/OLCI for band Oa17: 865nm over Mauritania-1 site. Dashed-green and orange lines indicate the 2% and 5% respectively. Error bars indicate the desert methodology uncertainty. -----28

Figure 33: The estimated gain values for S3A/OLCI from Glint, Rayleigh, and PICS over the period November 2016 – June 2017 as a function of wavelength. We use the gain value of Oa8 from Desert method as reference gain for Glint. Dashed-green and orange lines indicate the 2% and 5% respectively. Error bars indicate the methods uncertainties. -----29

Figure 34: OSCAR Libya-4 deserts results over the period March 2017 –June 2017 in function of wavelength. Only observations with VZA less than 30° are considered. The error bars indicate the standard deviation over the 21 observations. -----30

Figure 35: OTCI time series for DEGb site. -----32

Figure 36: OTCI time series for ITCat site. -----32

Figure 37: OTCI time series for ITIsp site. -----33

Figure 38: OTCI time series for ITSro site. -----33

Figure 39: OTCI time series for ITTra site. -----34

Figure 40: OTCI time series for SPAlI site. -----34

Figure 41: OTCI time series for SPVal site. -----35

Figure 42: OTCI time series for UKNfo site. -----35

Figure 43: OTCI time series for USNe1 site. -----36

Figure 44: OTCI time series for USNe2 site. -----36

Figure 45: OTCI time series for USNe3 site. -----37

Figure 46: Newforest study site for direct validation. -----37

Figure 47: High resolution Canopy chlorophyll content (mg m^{-2}) for the study site. -----38

Figure 48: Relationship between canopy chlorophyll content and OTCI over the study site -----39

Figure 49: Scatter plots of OLCI versus in situ radiometry -----41

Figure 50: OLCI and AERONET-OC radiometric time series AAOT station. -----43

Figure 51: OLCI and AERONET-OC radiometric time series Wave-CIS station. -----44

	<p>Sentinel-3 MPC</p> <p>S3-A OLCI Cyclic Performance Report</p> <p>Cycle No. 018</p>	<p>Ref.: S3MPC.ACR.PR.01-018</p> <p>Issue: 1.1</p> <p>Date: 22/06/2017</p> <p>Page: ix</p>
--	--	--

Figure 52: Profile of aerosol optical thickness T865 (upper left), an image of T865 with the yellow line for which T865 is retrieved (lower right), Ångström coefficient A865 (upper middle), OC4ME (lower left) and IWV (lower middle); the OLCI scene from 15.03.2017 (21:43.45-22:27.42) is at 9°37' N and 176° E.-----46

Figure 53: Profile of Ångström coefficient A865 (left), of CHL_OC4ME (middle), and of IWV (right), see Figure 52 for further details.-----46

Figure 54 Profile of aerosol optical thickness T865 (upper left), an image of T865 with the yellow line for which T865 is retrieved (lower right), Ångström coefficient A865 (upper right), and IWV (lower left); OLCI scene at 15°36' N and 178° E from 15.03.2017 (21:43.45-22:27.42).-----47

Figure 55: Profile of Ångström coefficient A865 (left) and of IWV (right), see Figure 54 for further details.48

Figure 56: Profile of aerosol optical thickness T865 (upper left), an image of T865 with the line for which T865 is retrieved (lower right) and the red arrow, pointing to the pixel for which the reflectance spectrum is displayed (lower left), Ångström coefficient A865 (upper middle), OC4ME (upper right) and IWV (lower middle); the OLCI scene from 15.03.2017 (21:43.45-22:27.42) is at 2°41' N and 173°54' E.--48

Figure 57: Profile of aerosol optical thickness T865 (upper middle), an image of T865 with the yellow line for which T865 is retrieved (lower right), Ångström coefficient A865 (upper right), and IWV (lower middle), the cloud flag is set (yellow); OLCI scene at 16° S and 102° E from 10.05.2017 (02:14.42-02:59.04).-----49

Figure 58: Profile of aerosol optical thickness T865 (upper middle), an image of T865 with the line for which T865 is retrieved (lower right), Ångström coefficient A865 (upper right), and IWV (lower middle); OLCI scene at 24° S and 66° W from 10.05.2017 (14:01.34-14:45.57).-----49

Figure 59: Profile of T865 (left) and IWV (right); OLCI scene at 24° S and 66° W from 10.05.2017 (14:01.34-14:45.57), see Figure 58.-----50

Figure 60: Profile of aerosol optical thickness T865 (upper left), an image of T865 with the yellow line for which T865 is retrieved (lower right), Ångström coefficient A865 (upper right), and IWV (lower middle); OLCI scene from 10.05.2017 (14:01.34-14:45.57).-----51



1 Instrument monitoring

1.1 CCD temperatures

The monitoring of the CCD temperatures is based on MPMF data extractions not yet operational. In the meantime, we monitor the CCD temperatures on the long-term using Radiometric Calibration Annotations (see Figure 1). Variations are very small (0.08 C peak-to-peak) and no trend can be identified. Data from current cycle (rightmost data points) do not show any specificity.

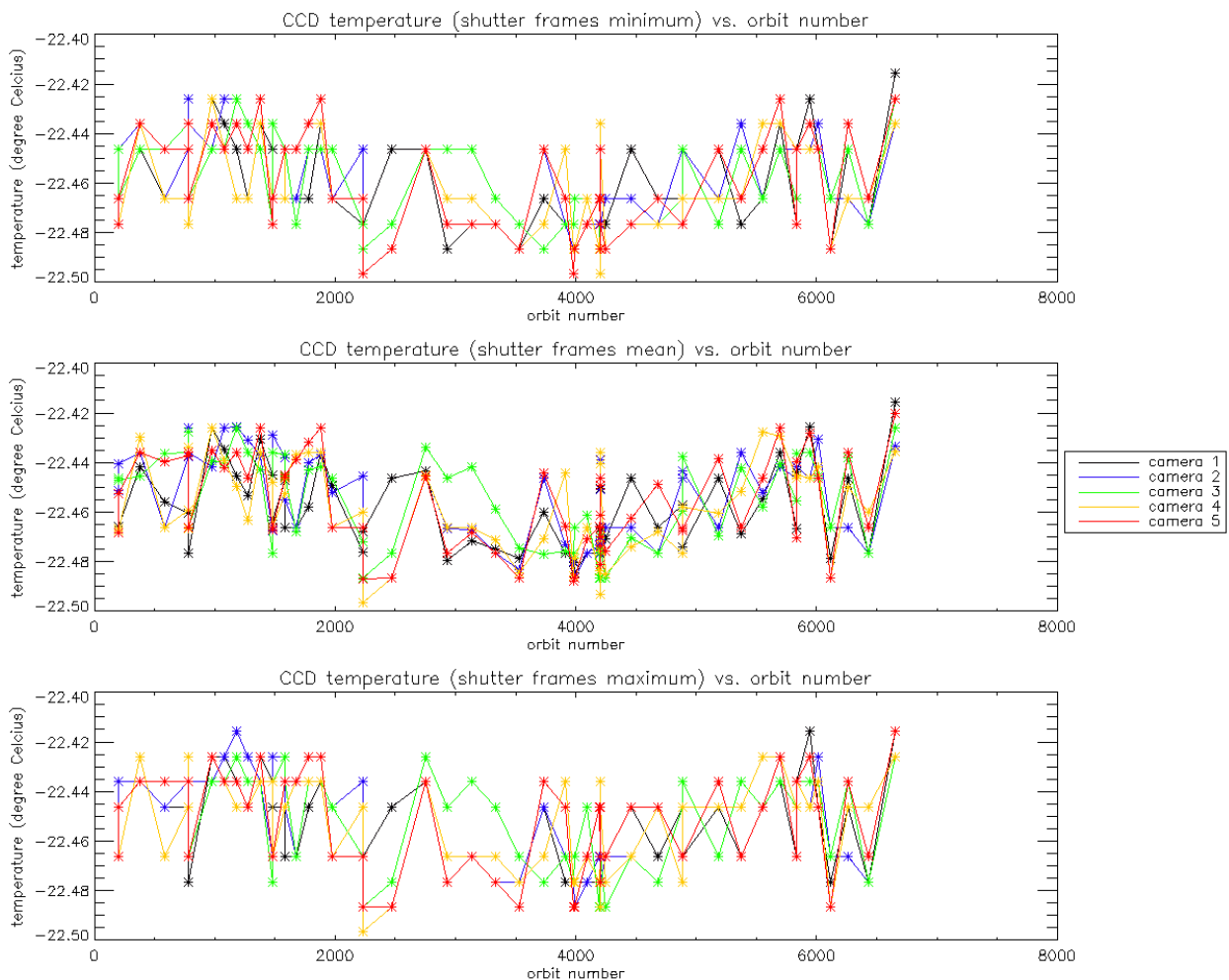


Figure 1: long term monitoring of CCD temperatures using minimum value (top), time averaged values (middle), and maximum value (bottom) provided in the annotations of the Radiometric Calibration Level 1 products, for the Shutter frames, all radiometric calibrations so far.

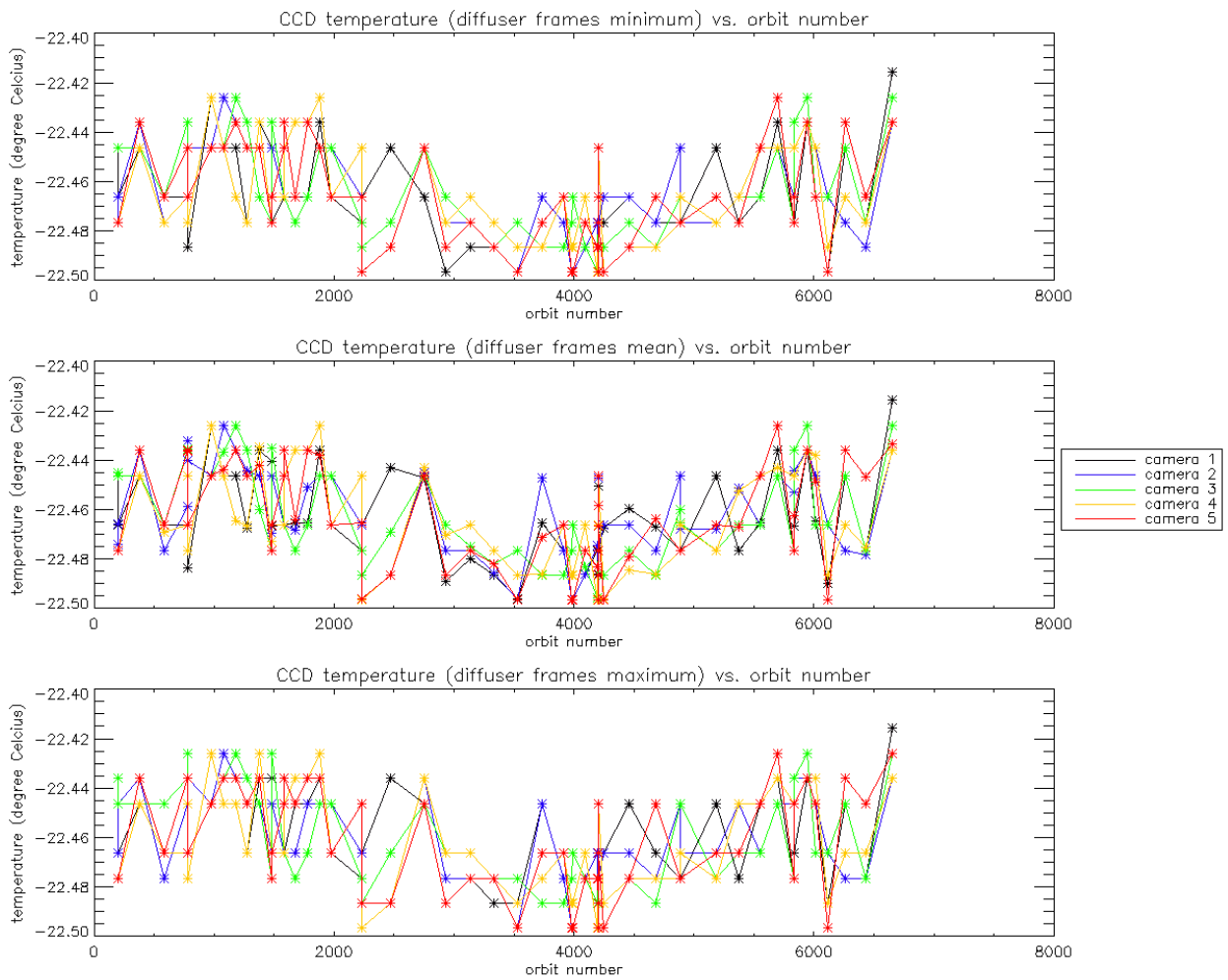


Figure 2: Same as Figure 1 for diffuser frames.

1.2 Radiometric Calibration

One OLCI Radiometric Calibration Sequence has been acquired during Cycle 018:

- ❖ S01 sequence on 28/05/2017 20:35 to 20:37 (absolute orbit 6653)

The acquired Sun azimuth angles are presented on below, on top of the nominal values without Yaw Manoeuvre (i.e. with nominal Yaw Steering control of the satellite).



Sentinel-3 MPC
S3-A OLCI Cyclic Performance Report
Cycle No. 018

Ref.: S3MPC.ACR.PR.01-018
 Issue: 1.1
 Date: 22/06/2017
 Page: 3

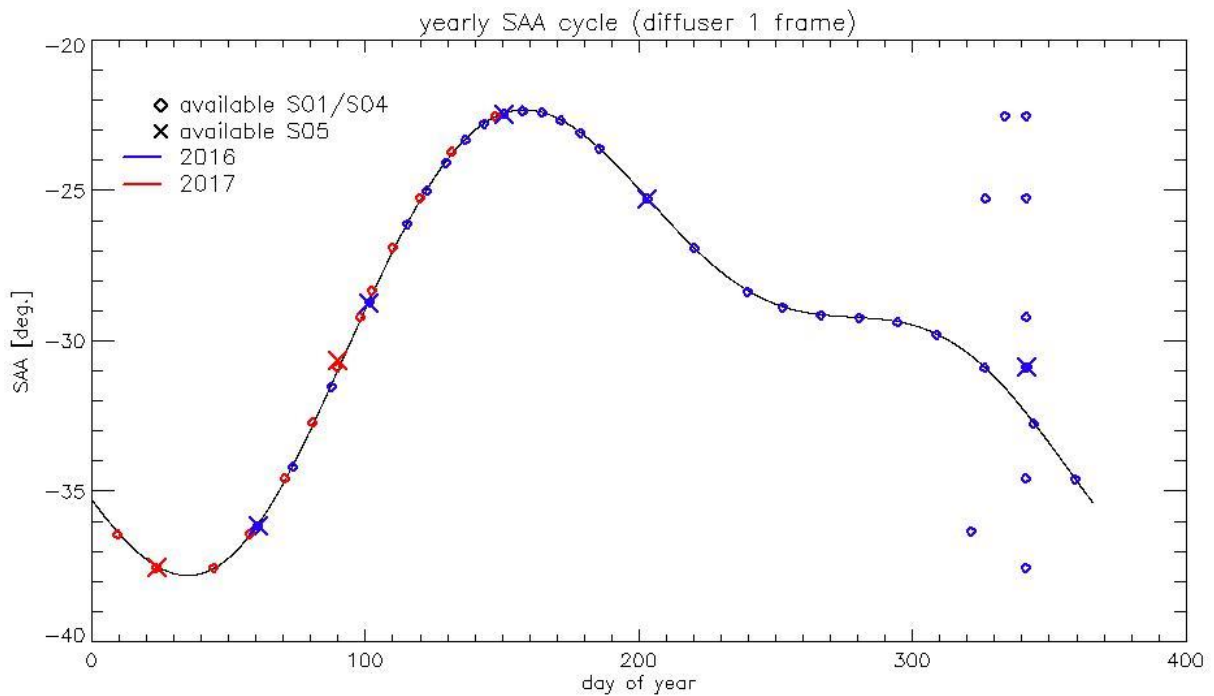


Figure 3: Sun azimuth angles during acquired Radiometric Calibrations (diffuser frame) on top of nominal yearly cycle (black curve). Diffuser 1 with diamonds, diffuser 2 with crosses, 2016 acquisitions in blue, 2017 in red.

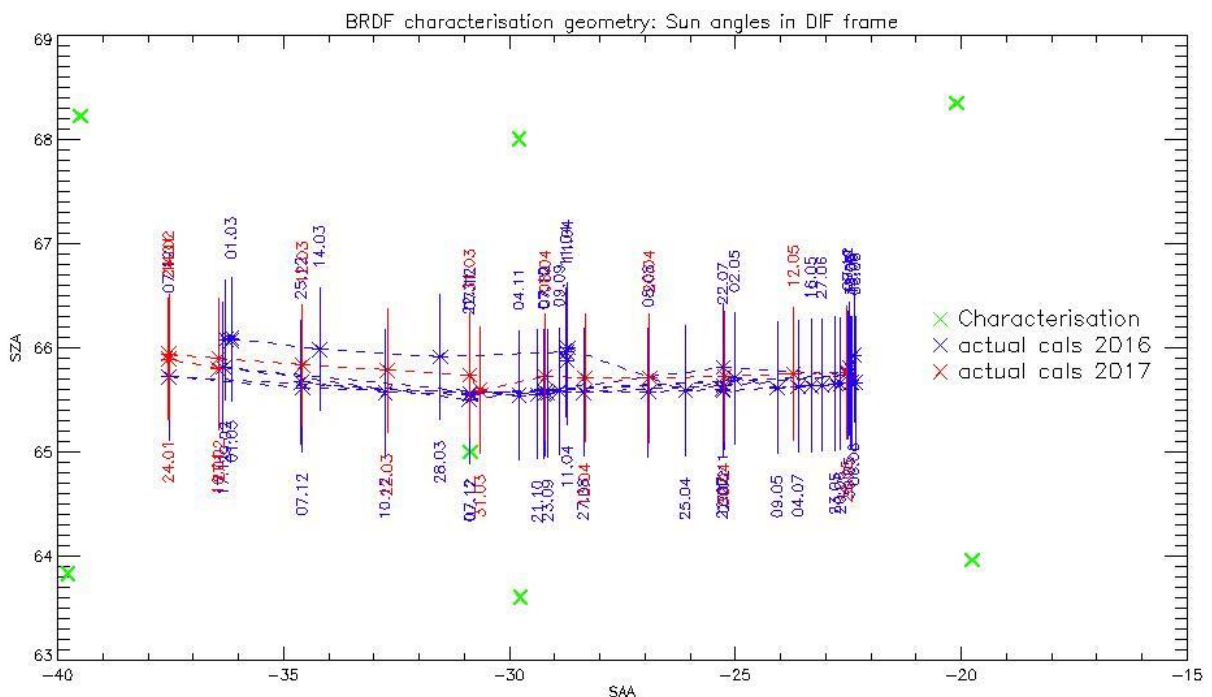


Figure 4: Sun geometry during radiometric Calibrations on top of characterization ones (diffuser frame)

This section presents the overall monitoring of the parameters derived from radiometric calibration data and highlights, if present, specificity of current cycle data.



1.2.1 Dark Offsets [OLCI-L1B-CV-230]

Dark offsets

Dark offsets are continuously affected by the global offset induced by the Periodic Noise on the OLCI convergence. Current Cycle calibrations (orbits 4685, 4887 & 4888) are affected the same way as others. The amplitude of the shift varies with band and camera from virtually nothing (e.g. camera 2, band 0a1) to up to 5 counts (0a21, camera 3). The Periodic Noise itself comes on top of the global shift with its known signature: high frequency oscillations with a rapid damp. This effect remains more or less stable with time in terms of amplitude, frequency and decay length, but its phase varies with time, introducing the global offset mentioned above.

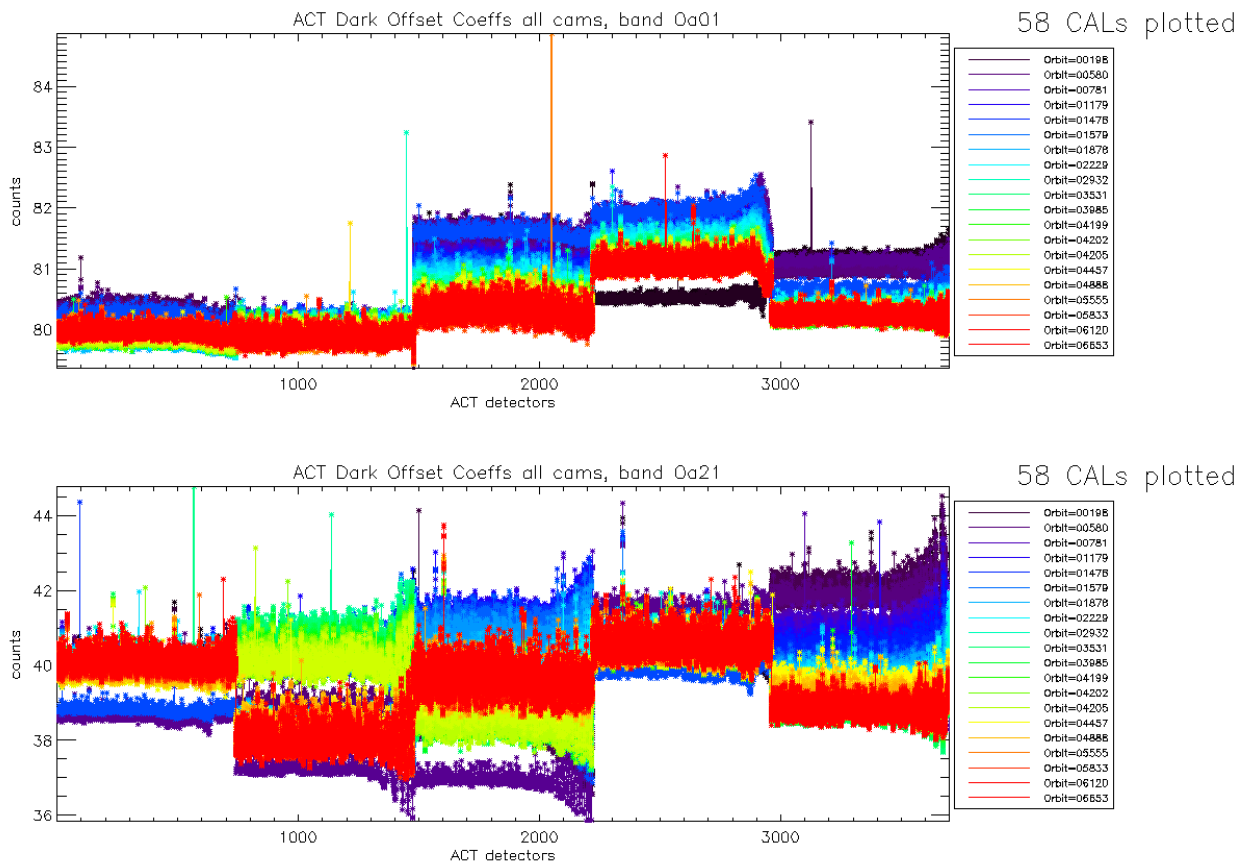


Figure 5: Dark Offset for band Oa1 (top) and Oa21 (bottom), all radiometric calibrations so far except the first one (orbit 183) for which the instrument was not thermally stable yet.

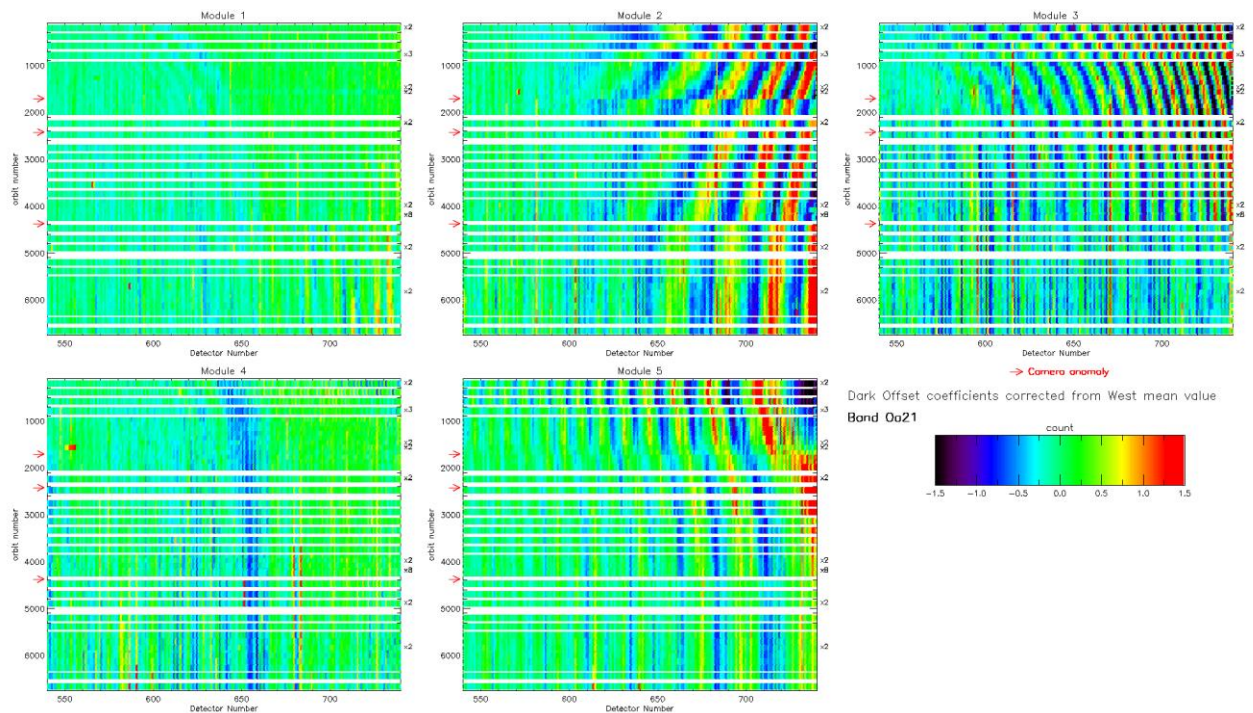


Figure 6: map of periodic noise for the 5 cameras, for band Oa21. X-axis is detector number (East part, from 540 to 740, where the periodic noise occurs), Y-axis is the orbit number. The counts have been corrected from the west detectors mean value (not affected by periodic noise). Periodic noise amplitude is high in camera 2, 3 and 4. It is lower in camera 4 and small in camera 1.

Looking at Figure 5 shows no significant evolution of this parameter during the current cycle. Figure 6 shows that since the last sudden PN change (phase and amplitude) caused by the camera-2 anomaly at orbit 4364 (18 December 2016), PN is nearly stabilized again. (See in particular cameras 2, 3 & 5).

Dark Currents

Dark Currents are not affected by the global offset of the Dark Offsets, thanks to the clamping to the average blind pixels value. However, the oscillations of Periodic Noise remain visible. There is no significant evolution of this parameter during the current cycle.

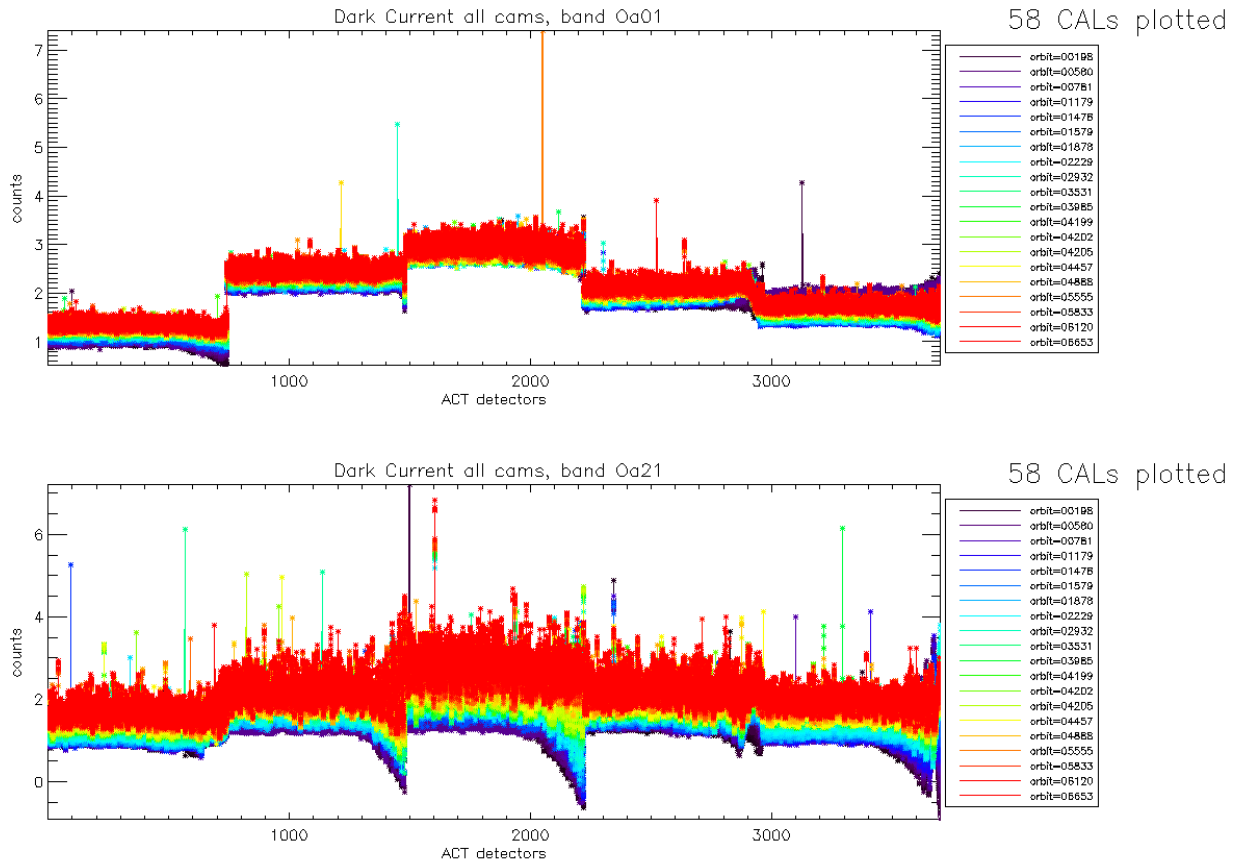


Figure 7: Dark Current for band Oa1 (top) and Oa21 (bottom), all radiometric calibrations so far except the first one (orbit 183) for which the instrument was not thermally stable yet.

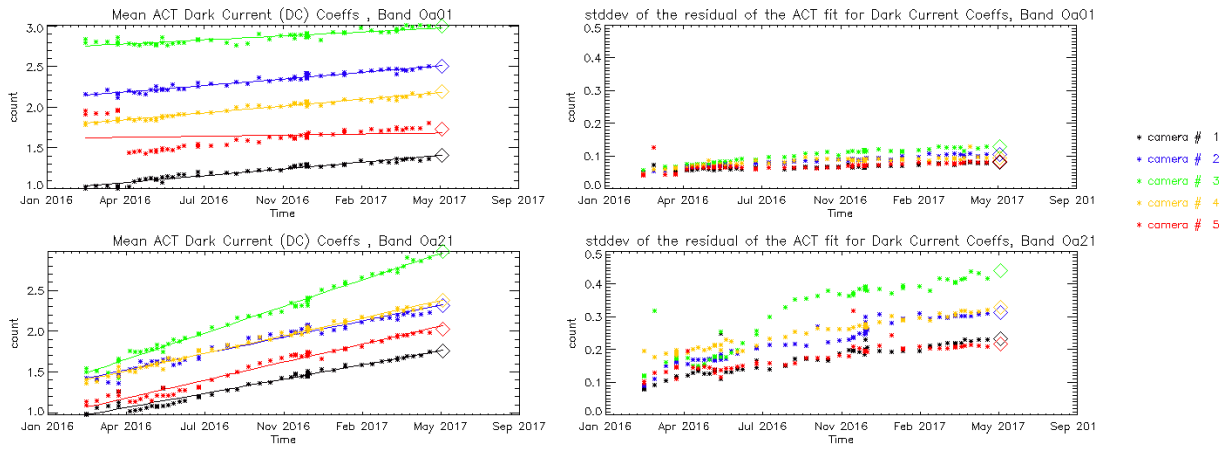


Figure 8: left column: ACT mean on 400 first detectors of Dark Current coefficients for spectral band Oa01 (top) and Oa21 (bottom). Right column: same as left column but for Standard deviation instead of mean. We see an increase of the DC level as a function of time especially for band Oa21. A possible explanation could be the increase of the number of hot pixels which is more important in Oa21 because this band is made of more CCD lines than band Oa01 and thus receives more cosmic rays impacts. It is known that cosmic rays degrade the structure of the CCD, generating more and more hot pixels at long term scales.

1.2.2 Instrument response and degradation modelling [OLCI-L1B-CV-250]

1.2.2.1 Instrument response monitoring

Figure 9 below shows the gain coefficients of every pixel for two OLCI channels, Oa1 (400 nm) and Oa21 (1020 nm), highlighting the significant evolution of the instrument response since early mission.

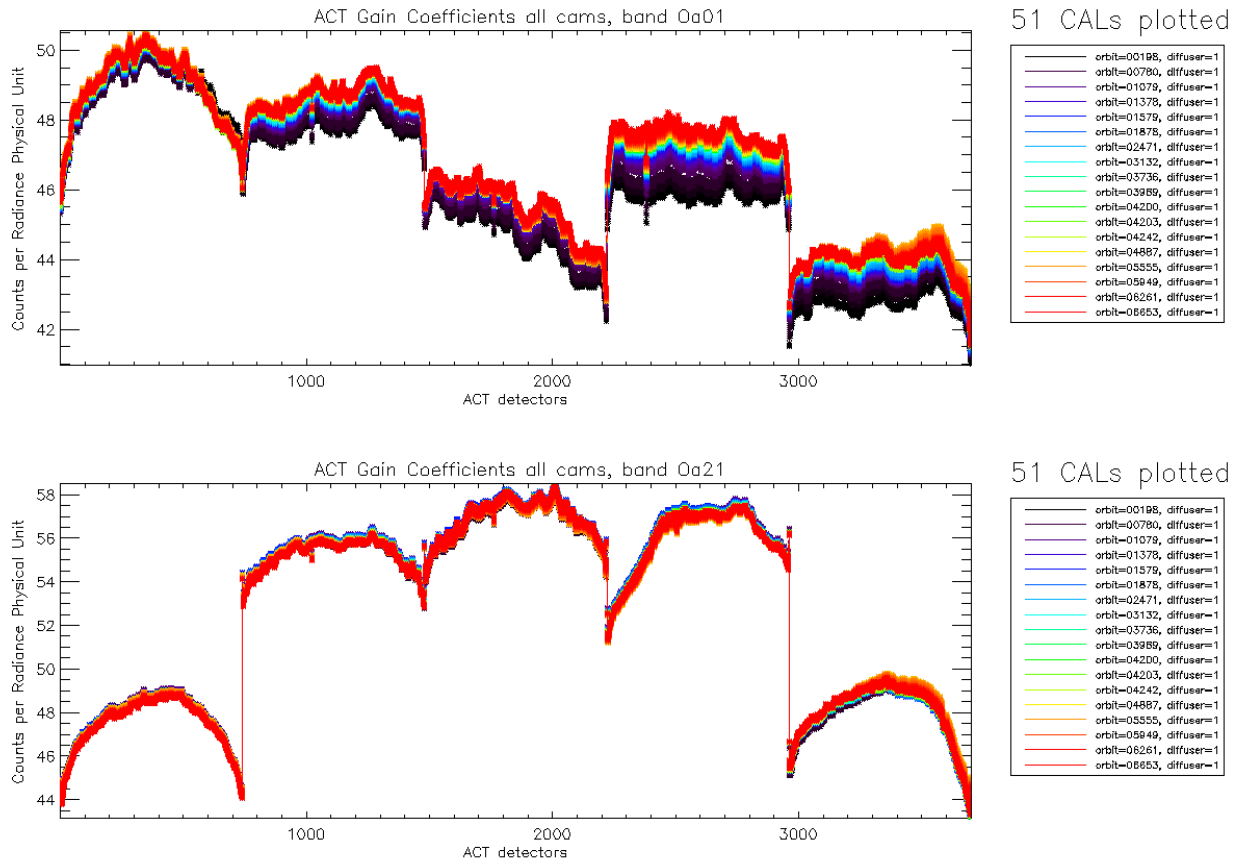


Figure 9: Gain Coefficients for band Oa1 (top) and Oa21 (bottom), all diffuser 1 radiometric calibrations so far except the first one (orbit 183) for which the instrument was not thermally stable yet.

The gains plotted in Figure 9, however are derived using the ground BRDF model – as the only one available in the operational processing software so far – which is known to suffer from illumination geometry dependent residual errors (see previous Cyclic Reports for more details). Consequently they are post-processed to replace the ground BRDF model by the in-flight version, based on Yaw Manoeuvres data, prior to determine the radiometric evolution.

Figure 10 displays a summary of the time evolution derived from post-processed gains: the cross-track average of the BRDF corrected gains is plotted as a function of time, for each module, relative to a given reference calibration (the 12/12/2016). It shows that, if a significant evolution occurred during the early mission, the trends tend to stabilize, with the exception of band 1 of camera 4.

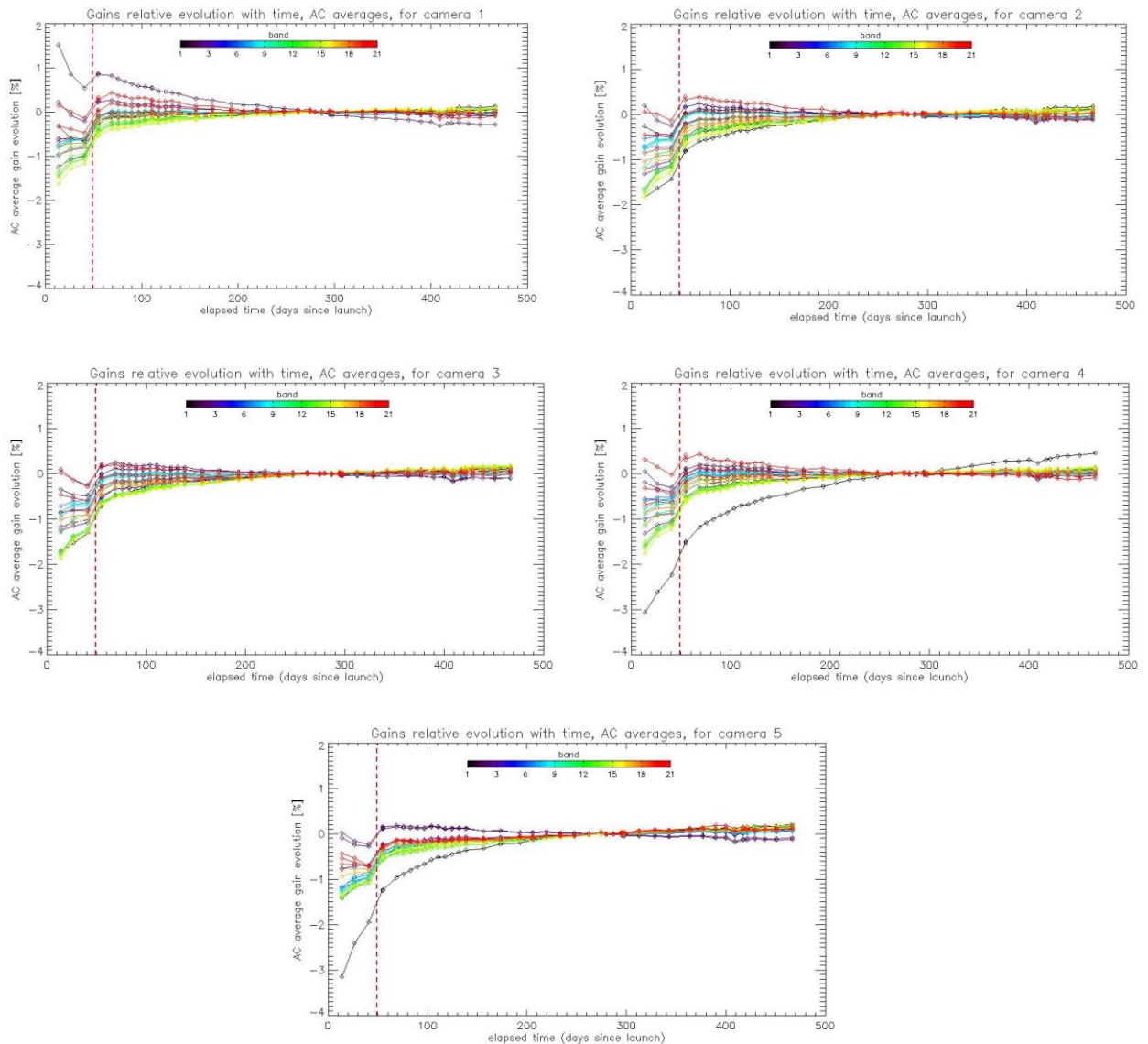


Figure 10: camera averaged gain relative evolution with respect to “best geometry” calibration (22/11), as a function of elapsed time since launch; one curve for each band (see colour code on plots), one plot for each module. The star tracker anomaly fix (6/04/16) is represented by a vertical red dashed line.

The behaviour over the first two months of mission, really different and highlighted by Figure 10, is explained by the Star Tracker software anomaly during which the attitude information provided by the platform was corrupted, preventing to compute a correct illumination geometry, with a significant impact on the gain computation.

1.2.2.2 Instrument evolution modelling

Thanks to the work done on the Yaw Manoeuvres Calibration acquisitions (see section 1.2.5) an upgraded diffuser BRDF model has been derived, allowing to get rid of the operational model dependency with Sun azimuth discussed above. This in turn allowed building a global gain database

corrected for BRDF error residuals. This database was used as the basis for the derivation of a long-term radiometric drift model.

This required a number of adaptations of the dedicated software for several reasons:

- 1) The upgraded BRDF model is not implemented in the Calibration processing software (IPF OL1-RC), thus the derived gains have to be corrected for BRDF in a post-processing step, on the (justified) assumption that the BRDF changes have a second order impact on the stray-light computation.
- 2) The observed instrument evolution does not follow the expected behaviour: a slow and smooth instrument sensitivity decrease, but on the contrary can show increase as well (see Figure 11))
- 3) The time period is not long enough to correctly model the evolution for cameras/channels for which it is very small: in this case the signal to noise ratio (e. g. due to diffuser speckle) is not high enough and the fit parameters that provide the best match are not physical. As a consequence, it may happen that, despite the model matches very well to the data, its use in extrapolation generates huge drifts that are very unlikely to occur. A post-processing is thus necessary to identify and update those cases.

The model has been derived from the dataset ranging from 26/04/2016 to 12/03/2017, so that the validation dataset now includes 8 calibrations over 2.5 months for performance estimation, including the calibrations acquired during current cycle.

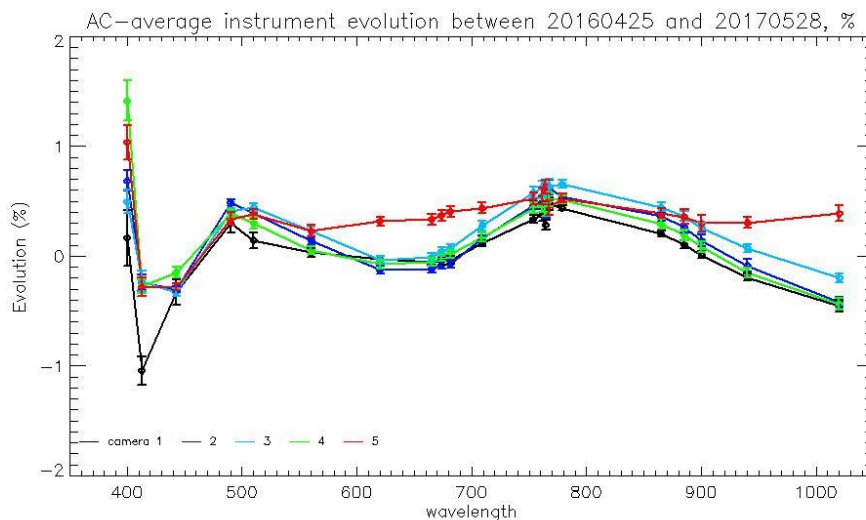


Figure 11: Camera-averaged instrument evolution since channel programming change (25/04/2016) and up to most recent calibration (28/05/2017) versus wavelength.

Once these steps are completed, the model performance over the complete dataset (including 8 calibrations in extrapolation over up to 2.5 months) is better than 0.2% except at very specific cases: few isolated pixels in about half of the bands, and two specific features in camera 5 for channels Oa8 and Oa21 that cannot be fitted with a bounded exponential model. The overall performance at each orbit is



shown on Figure 12 as the average and standard deviation of the model over data ratio as a function of wavelength, for each orbit in order to highlight a possible extrapolation issue. If the figure shows an outlying orbit, it must be stressed that it is NOT the most recent, excluding a systematic drift in extrapolation, as proved by Figure 13.

Finally, Figure 14 to Figure 16 show the detail of the model performance, with across-track plots of the model over data ratios at each orbit, one plot for each channel.

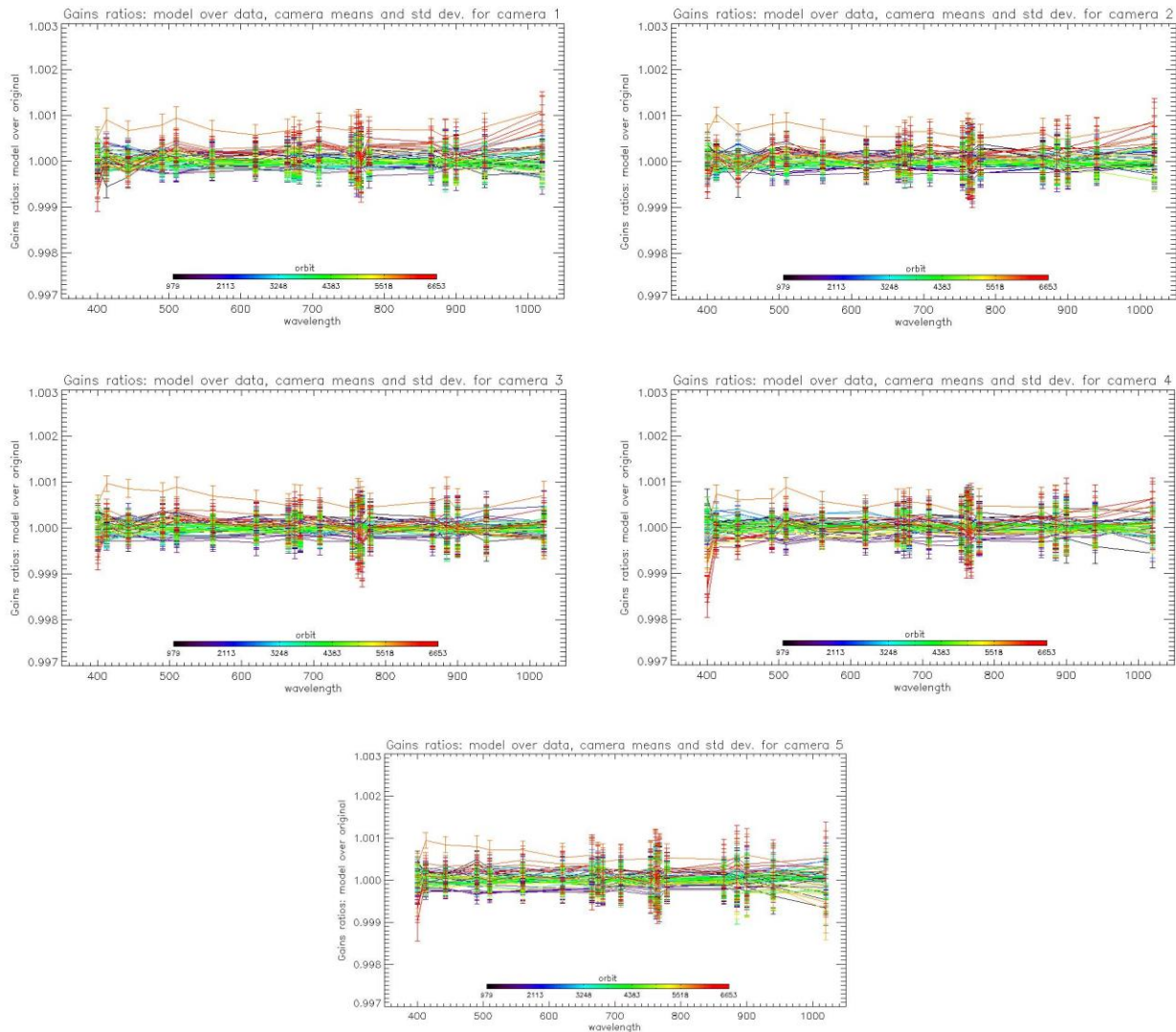


Figure 12: For the 5 cameras: Evolution model performance, as camera-average and standard deviation of ratio of Model over Data vs. wavelength, for each orbit of the test dataset, including 8 calibration in extrapolation, with a colour code for each calibration from blue (oldest) to red (most recent).

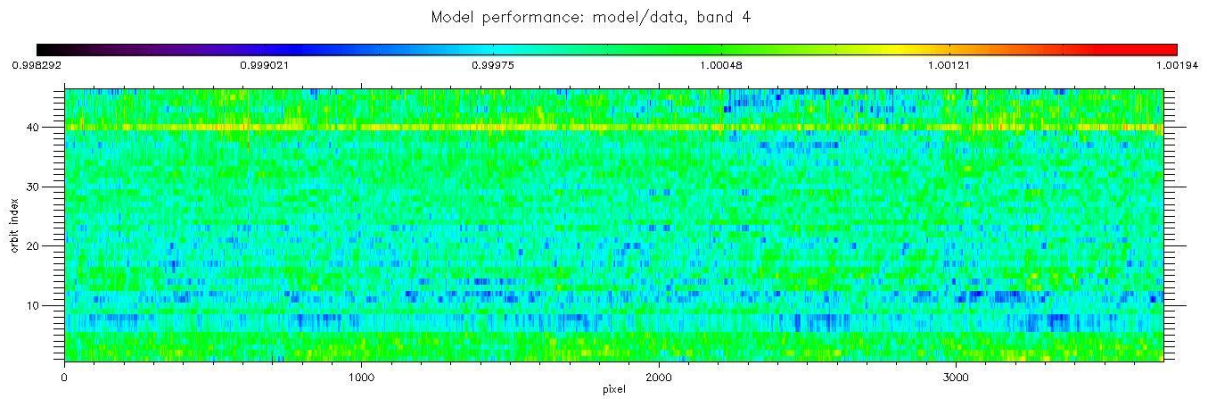


Figure 13: model performance: ratio of model over data for all pixels (x axis) of all orbits (y axis), for channel Oa4. The outlying orbit #40 is that of 31/03/2017.

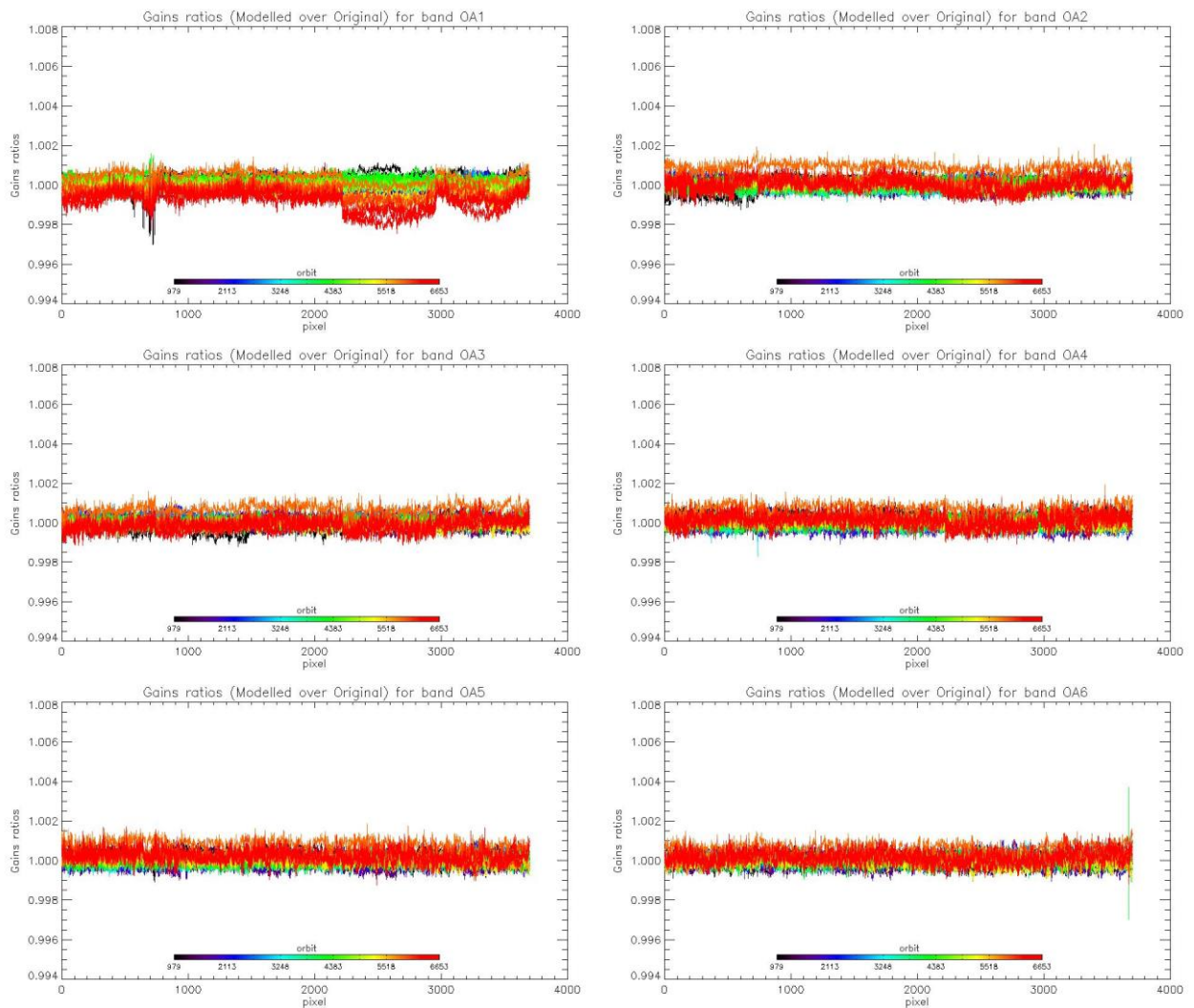


Figure 14: Evolution model performance, as ratio of Model over Data vs. pixels, all cameras side by side, over the whole current calibration dataset (since instrument programming update), including 8 calibration in extrapolation, channels Oa1 to Oa6.



Sentinel-3 MPC
S3-A OLCI Cyclic Performance Report
Cycle No. 018

Ref.: S3MPC.ACR.PR.01-018
Issue: 1.1
Date: 22/06/2017
Page: 13

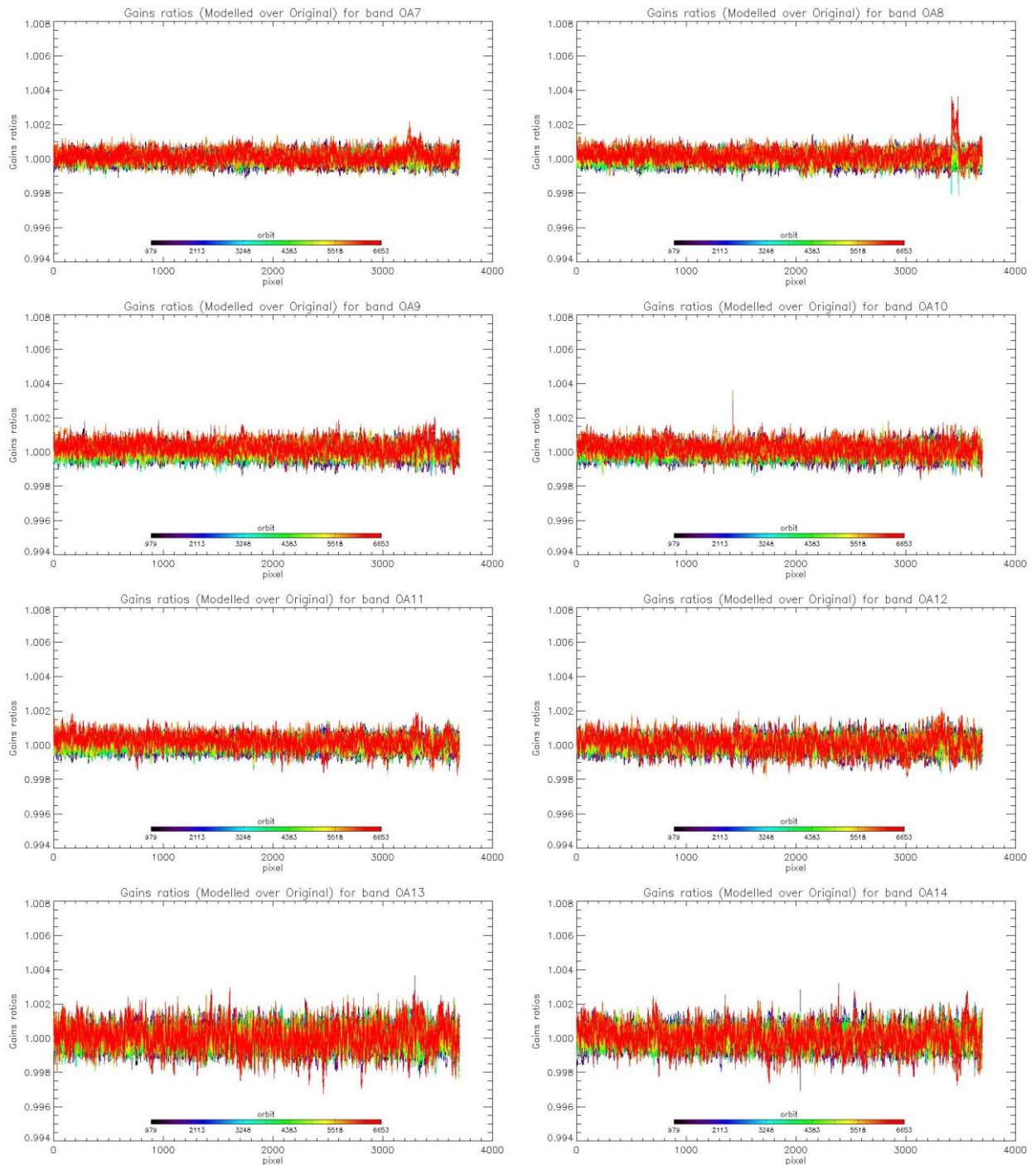


Figure 15: same as Figure 14 for channels Oa7 to Oa14.



Sentinel-3 MPC
S3-A OLCI Cyclic Performance Report
Cycle No. 018

Ref.: S3MPC.ACR.PR.01-018
Issue: 1.1
Date: 22/06/2017
Page: 14

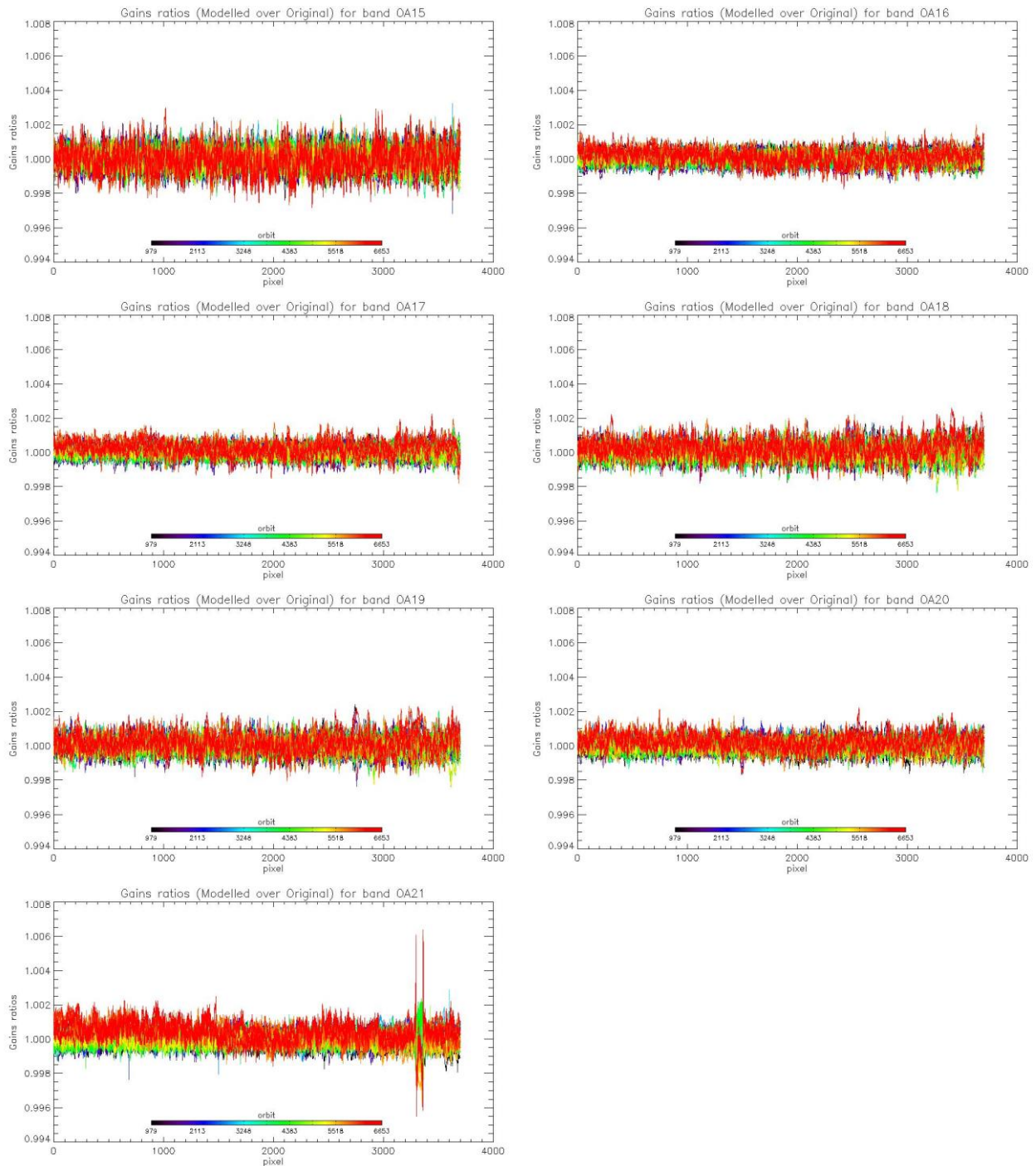


Figure 16: same as Figure 14 for channels Oa15 to Oa21.

1.2.3 Ageing of nominal diffuser [OLCI-L1B-CV-240]

There has been no calibration sequence S05 (reference diffuser) acquisition during cycle 018.

Consequently the last updated results are still valid and reported below.

The diffuser 1 Ageing is computed for each 3700 detector and each spectral band by formula:

$$\text{Ageing}(\text{orb}) = G1(\text{orb})/G2(\text{orb}) - G1(\text{orb_ref})/G2(\text{orb_ref})$$

Where:

- ❖ G1 is the diffuser 1 (= nominal diffuser) Gain coefficients.
- ❖ G2 is the diffuser 2 (= reference diffuser) Gain coefficients
- ❖ orb_ref is a reference orbit chosen at the beginning of the mission

Ageing is represented in Figure 17 for band Oa1 and in Figure 18 for band Oa16. The negative shift of the latest sequence (for which a slight increase would be expected instead) is not explained so far and still under investigation. It should be noted that the corresponding orbit of diffuser 1 (nominal) has also been detected as an outlier in the modelling of the radiometric long-term trend (see section 1.2.2.2) with an unexpected excess of brightness.

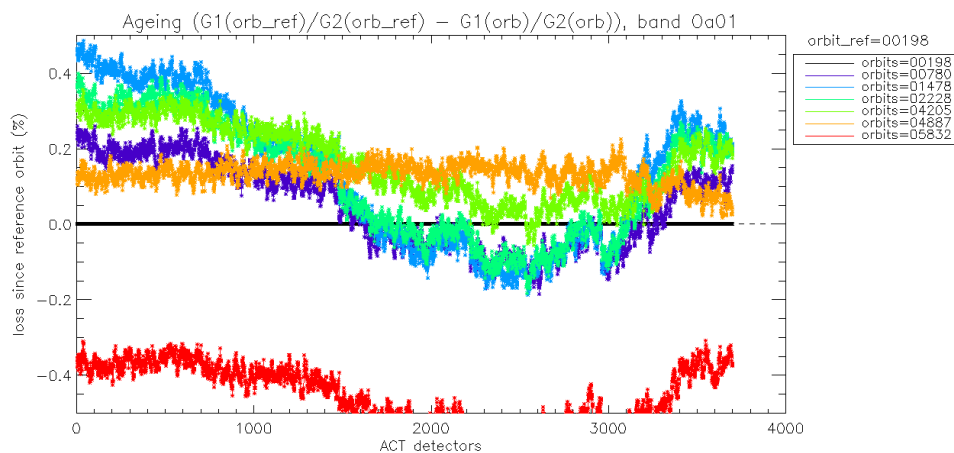


Figure 17: diffuser 1 ageing for spectral band Oa01. We see strong ACT low frequency structures that are due to residual of BRDF modelling.

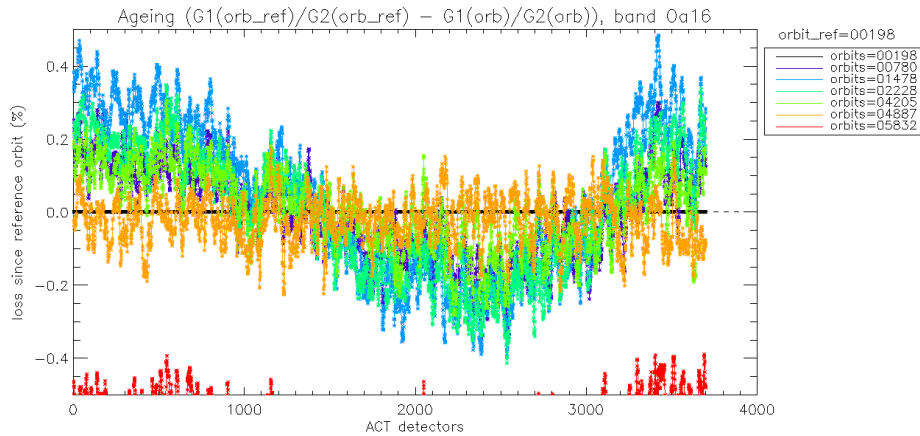


Figure 18: same as Figure 17 for spectral band Oa16. We use this band in order to normalize other bands and remove the ACT structures due to residual of BRDF modelling. Normalized curve for spectral band Oa01 is presented in Figure 19.

Figure 17 and Figure 18 show that the Ageing curves are impacted by a strong ACT pattern which is due to residuals of the bad modelling of the diffuser BRDF. This pattern is dependant of the azimuth angle. It is a 'white' pattern which means it is the same for all spectral bands. As such, we can remove this pattern by normalizing the ageing of all bands by the curve of band Oa16 which is expected not to be impacted by ageing because in the red part of the spectrum. We use an ACT smoothed version (window of 100 detectors) of band Oa16 in order to reduce the high frequency noise. Normalized ageing for spectral band Oa01 is represented in Figure 19 where we can see that this band is impacted by ageing of the diffuser.

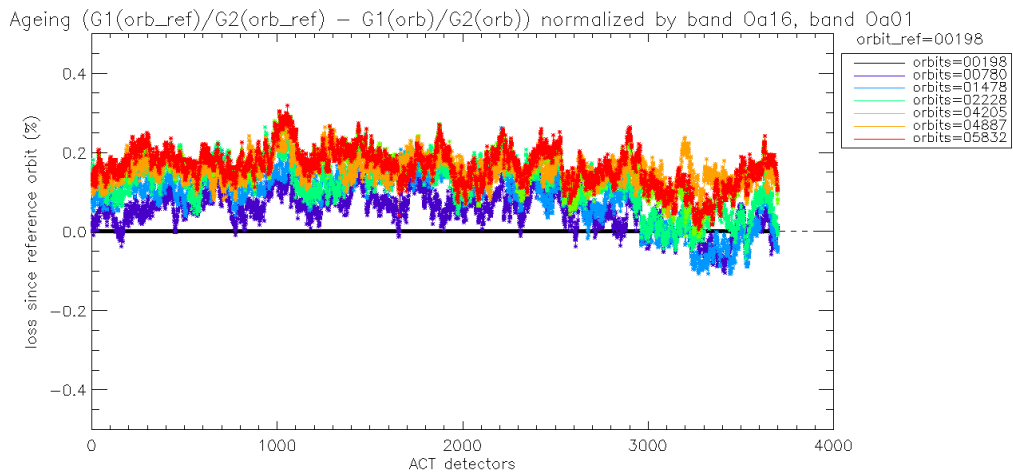


Figure 19: same as Figure 17 after normalization by band Oa16. Ageing of the diffuser 1 is now visible in the 5 cameras.



Camera averaged ageing (normalized by band Oa16) as a function of wavelength is represented in Figure 20 where we can see that ageing is stronger in the 'blue' (short wavelengths). Ageing is visible only for the 5 first spectral bands so far in the OLCI mission life.

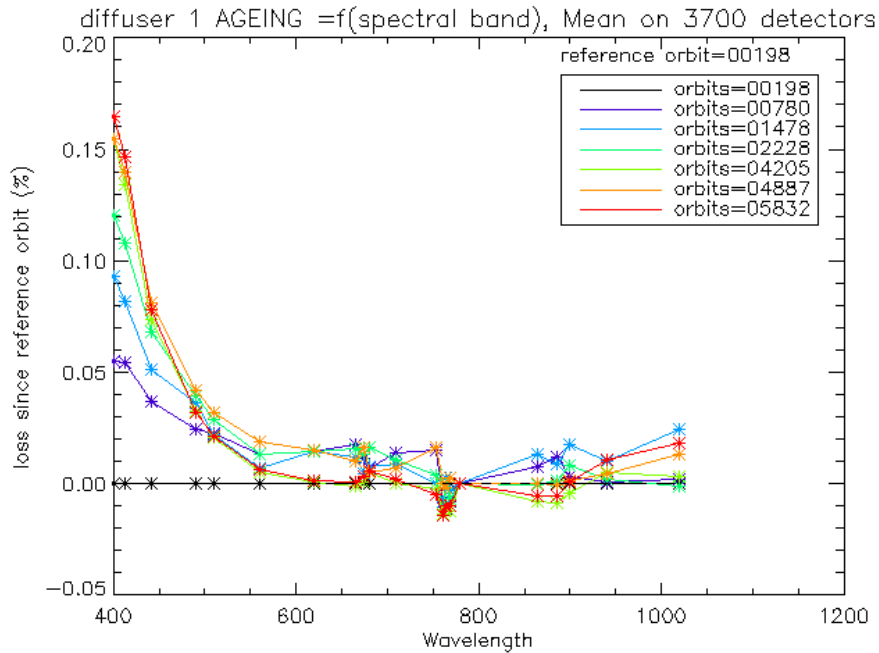


Figure 20: Diffuser 1 ageing as a function of wavelength (or spectral band). Ageing is visible in spectral band #1 to #5.

Figure 21 shows the evolution of the 5 camera averaged ageing as a function of time.

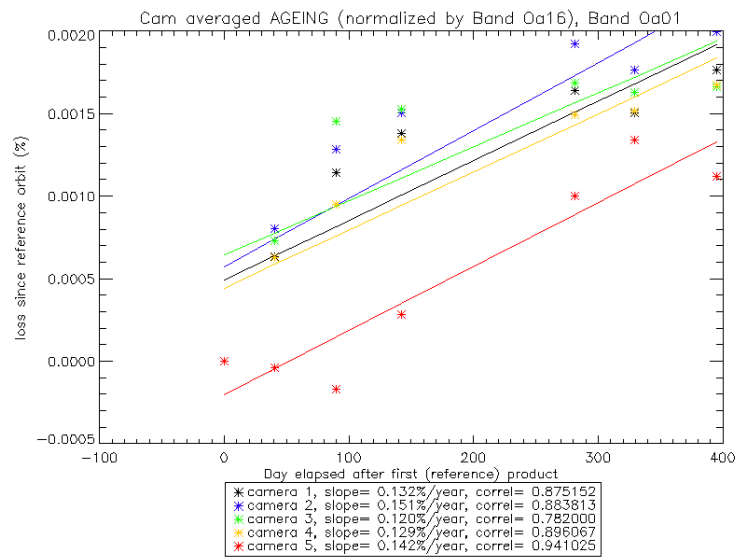


Figure 21: Camera averaged ageing (normalized by band Oa16) as a function of time. Linear fit for each camera is plotted. The slope (% loss per year) and the correlation coefficient of the linear fits are written in the legend at the bottom.

1.2.4 Updating of calibration ADF [OLCI-L1B-CV-260]

There has been no OL_1_CAL_AX generated during cycle 018.

1.2.5 Radiometric Calibrations for sun azimuth angle dependency and Yaw Manoeuvres for Solar Diffuser on-orbit re-characterization [OLCI-L1B-CV-270 and OLCI-L1B-CV-280]

This activity has not evolved during cycle 018 and results presented in previous report are still valid.

1.3 Spectral Calibration [OLCI-L1B-CV-400]

There have been two Spectral Calibration acquisitions during cycle 018.

One S02/S03 (Erbium doped diffuser):

- ❖ S02 sequence on 26/05/2017 07:46 to 07:48 (absolute orbit 6624)
- ❖ S03 sequence on 26/05/2017 09:27 to 09:29 (absolute orbit 6625)

And one S09 (Fraunhofer lines)

- ❖ S09 sequence on 26/05/2017 09:00 to 09:04 (absolute orbit 6625)

The long term evolution of spectral calibration obtained with calibration sequence S02/S03 is presented in Figure 22 and Figure 23 and the one obtained with calibration sequence S09 is presented in Figure 24.



Sentinel-3 MPC
S3-A OLCI Cyclic Performance Report
Cycle No. 018

Ref.: S3MPC.ACR.PR.01-018
Issue: 1.1
Date: 22/06/2017
Page: 19

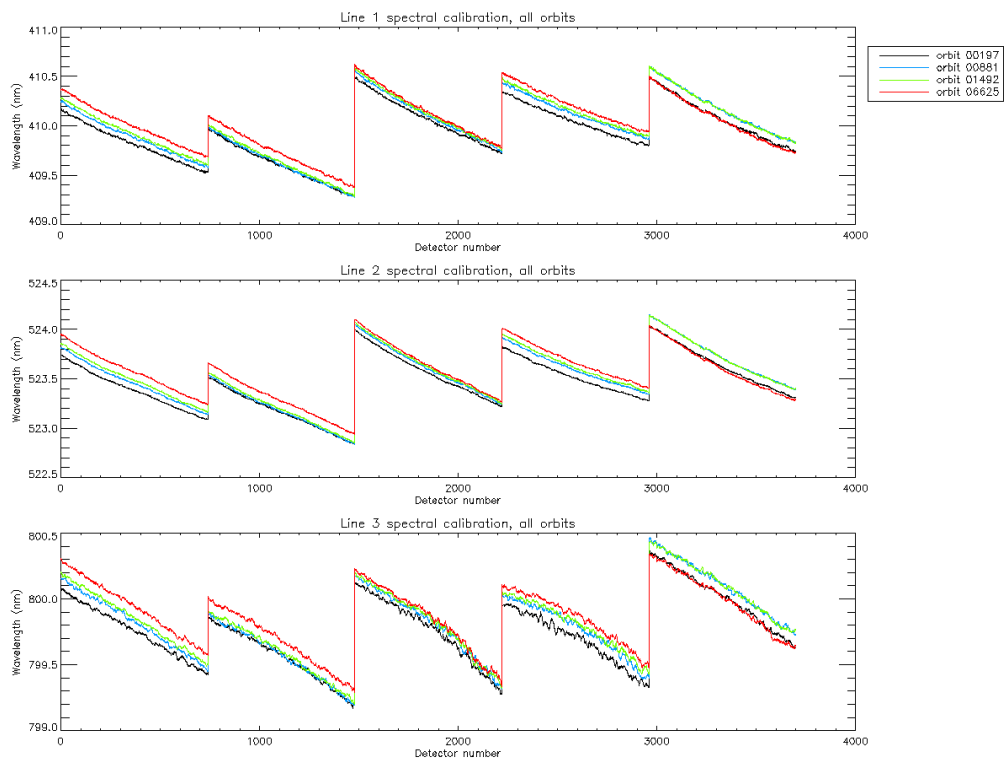


Figure 22: across track spectral calibration for all S02/S03 sequences since the beginning of the mission. Top plot is spectral line 1, middle plot is spectral line 2 and bottom plot spectral line 3.



Sentinel-3 MPC

S3-A OLCI Cyclic Performance Report

Cycle No. 018

Ref.: S3MPC.ACR.PR.01-018
 Issue: 1.1
 Date: 22/06/2017
 Page: 20

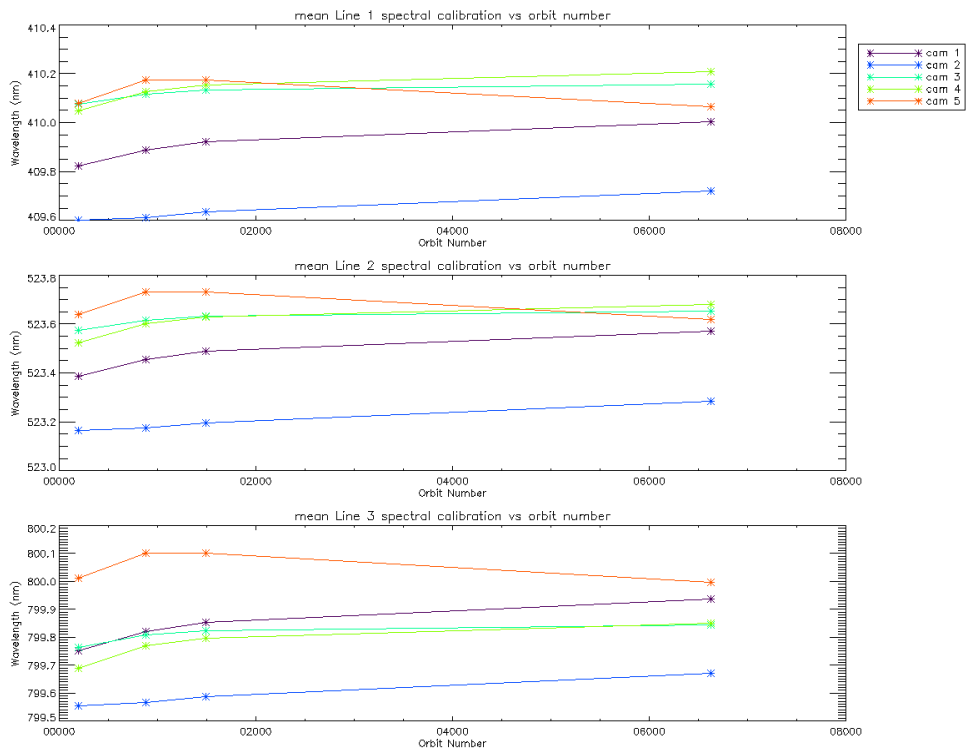


Figure 23: camera averaged spectral calibration as a function of orbit number (all spectral S02/S03 calibrations since the beginning of the mission are included). Top plot is spectral line 1, middle plot is spectral line 2 and bottom plot spectral line 3.

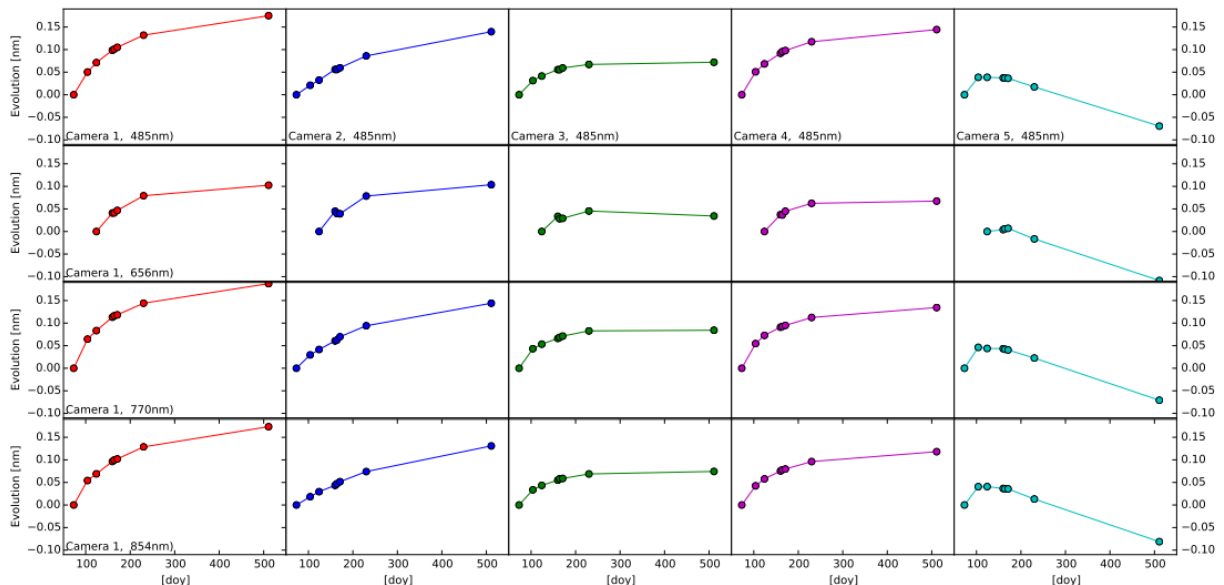


Figure 24: spectral calibration as a function of time derived from all S09 sequences. From left to right column: the 5 cameras. From top to bottom: Used absorption line: 485 nm, 656 nm, 770 nm and 854 nm.

We see that the long term evolution of the spectral calibration obtained with sequence S09 (Figure 24) is in rather good agreement with the one obtained with sequence S02/S03 (Figure 23). Indeed, we

	<p>Sentinel-3 MPC</p> <p>S3-A OLCI Cyclic Performance Report</p> <p>Cycle No. 018</p>	<p>Ref.: S3MPC.ACR.PR.01-018</p> <p>Issue: 1.1</p> <p>Date: 22/06/2017</p> <p>Page: 21</p>
--	--	--

observe for both methods a general positive trend of the spectral calibration for camera 1, 2, 3 and 4 with a kind of stabilization at the end for camera 3. An obvious negative trend is present in camera 5 also in both methods.

In all cases, the spectral calibration drift is smaller than 0.2 nm and the change with respect to the values included in the Auxiliary Data files is less than 0.1 nm. However camera 5, and to a lesser extend cameras 1 2 and 4, do further evolve thus and an evolution of the Auxiliary Parameters impacted by the instrument spectral model, reflecting the current state of the instrument, has to be considered.

1.4 Signal to Noise assessment [OLCI-L1B-CV-620]

1.4.1 SNR from Radiometric calibration data.

SNR computed for all calibration data as a function of band number is presented in Figure 25.

SNR computed for all calibration data as a function of orbit number for band Oa01 (the less stable band) is presented in Figure 26.

There is no significant evolution of this parameter during the current cycle and the ESA requirement is fulfilled for all bands.



Sentinel-3 MPC
S3-A OLCI Cyclic Performance Report
Cycle No. 018

Ref.: S3MPC.ACR.PR.01-018
 Issue: 1.1
 Date: 22/06/2017
 Page: 22

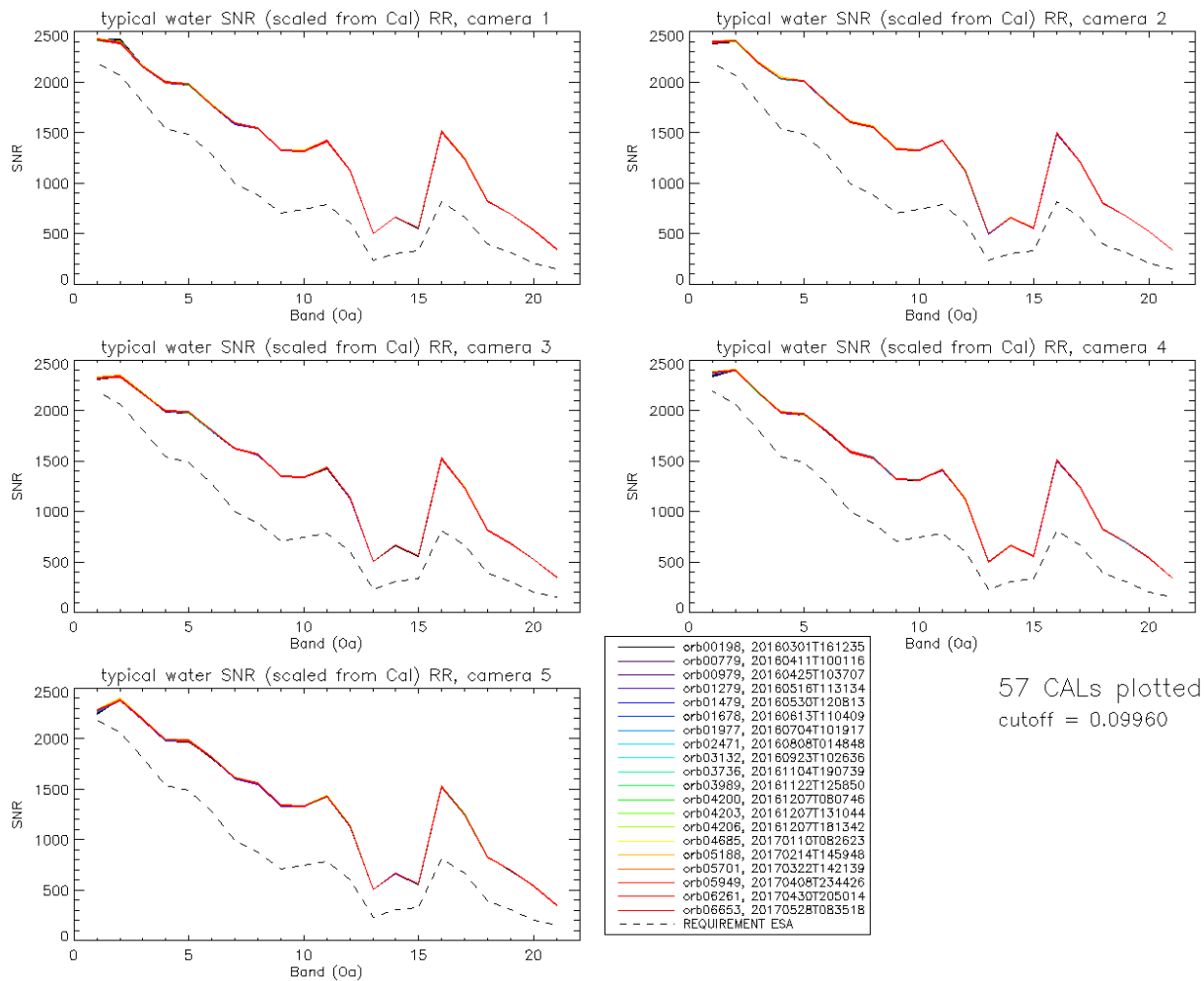


Figure 25: Signal to Noise ratio as a function of the spectral band for the 5 cameras. These results have been computed from radiometric calibration data. All calibrations except first one (orbit 183) are presents with the colours corresponding to the orbit number (see legend). The SNR is very stable with time: the curves for all orbits are almost superimposed. The dashed curve is the ESA requirement.

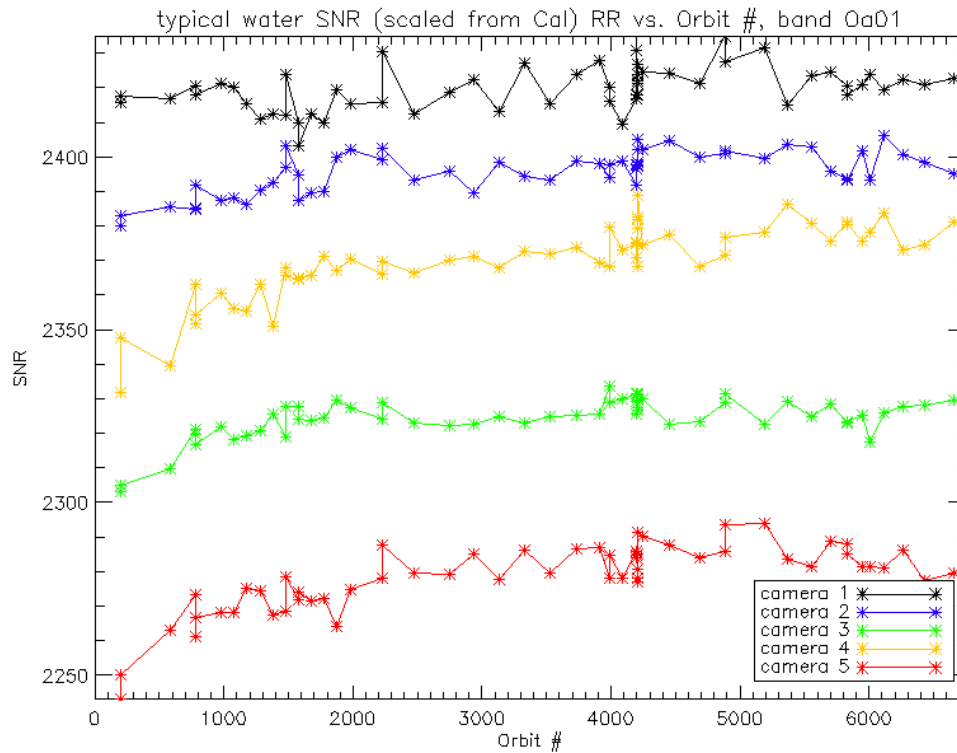


Figure 26: long-term stability of the SNR estimates from Calibration data, example of channel Oa1.

1.4.2 SNR from EO data.

There has been no update on SNR assessment from EO data during the cycle. Last figures (cycle 9) are considered valid.

1.5 Geometric Calibration/Validation

The Validation version GeoCal Tool implemented within the MPMF is now operational and used to monitor OLCI geometric performance. June results confirm very good performance. Monitoring of the geolocation performance by correlation with GCP imageries using the GeoCal tool over the period confirms that OLCI is compliant with its requirement: the centroid of the geolocation error is around 0.2 pixel in both along-track and across-track directions (Figure 27: histograms of geolocation errors for the along-track (left) and across-track (right) directions).

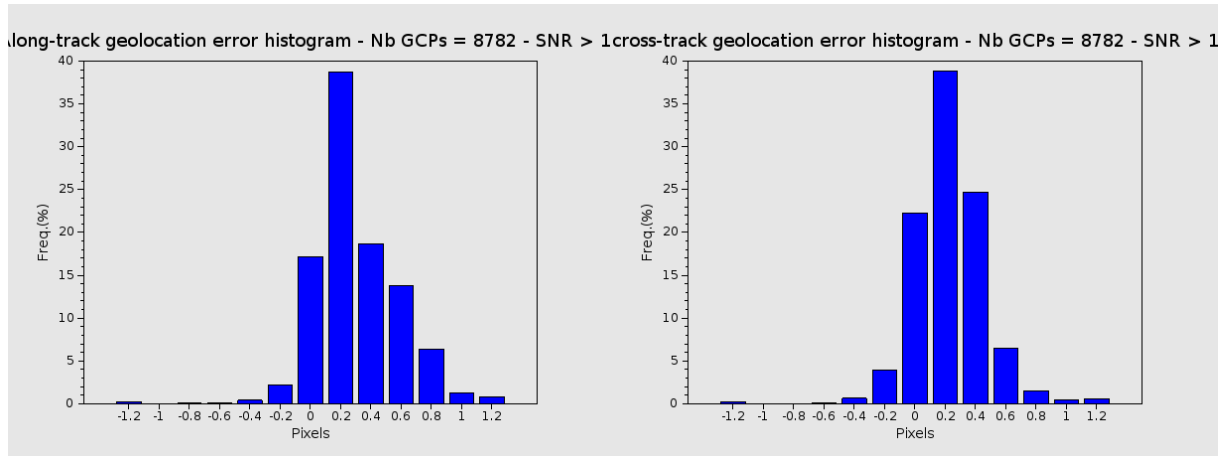


Figure 27: histograms of geolocation errors for the along-track (left) and across-track (right) directions.

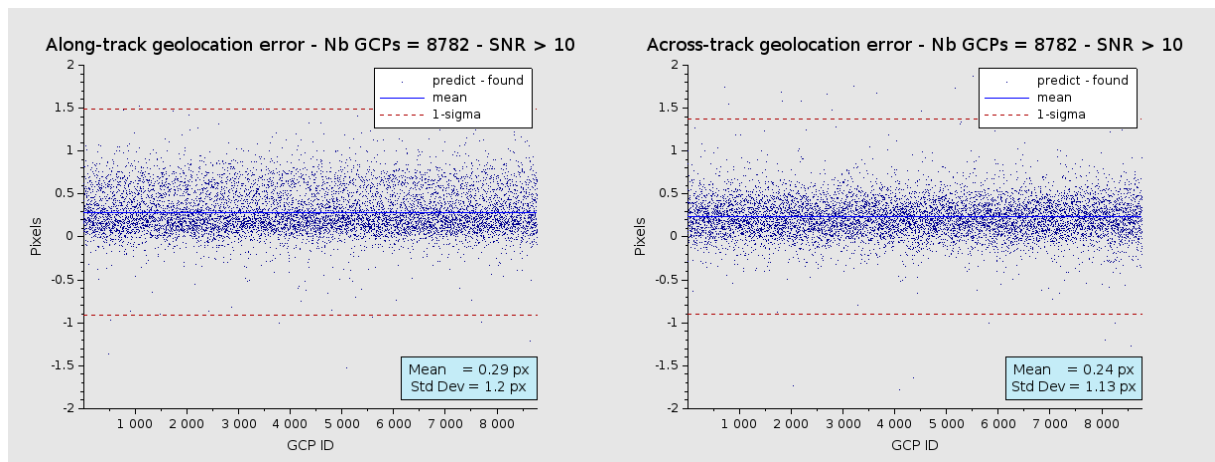


Figure 28: georeferencing error in along-track (left) and across-track (right) directions for all the GCPs.

The series plots of along-track and across-track georeferencing errors (Figure 28) show the pretty good stability of the geometric calibration but also highlight the significant number of outliers, despite the filtering on correlation level (SNR).

	Sentinel-3 MPC S3-A OLCI Cyclic Performance Report Cycle No. 018	Ref.: S3MPC.ACR.PR.01-018 Issue: 1.1 Date: 22/06/2017 Page: 25
--	---	---

2 OLCI Level 1 Product validation

2.1 [OLCI-L1B-CV-300], [OLCI-L1B-CV-310] – Radiometric Validation

2.1.1 S3ETRAC Service

Activities done

The S3ETRAC service extracts OLCI L1 RR and SLSTR L1 RBT data and computes associated statistics over 49 sites corresponding to different surface types (desert, snow, ocean maximizing Rayleigh signal, ocean maximizing sunglint scattering and deep convective clouds). The S3ETRAC products are used for the assessment and monitoring of the L1 radiometry (optical channels) by the ESLs.

All details about the S3ETRAC/OLCI and S3ETRAC/SLSTR statistics are provided on the S3ETRAC website <http://s3etrac.acri.fr/index.php?action=generalstatistics>

- ❖ Number of OLCI products processed by the S3ETRAC service
- ❖ Statistics per type of target (DESERT, SNOW, RAYLEIGH, SUNGLINT and DCC)
- ❖ Statistics per sites
- ❖ Statistics on the number of records

For illustration, we provide below statistics on the number of S3ETRAC/OLCI records generated per type of targets (DESERT, SNOW, RAYLEIGH, SUNGLINT and DCC).



Sentinel-3 MPC

S3-A OLCI Cyclic Performance Report

Cycle No. 018

Ref.: S3MPC.ACR.PR.01-018
 Issue: 1.1
 Date: 22/06/2017
 Page: 26

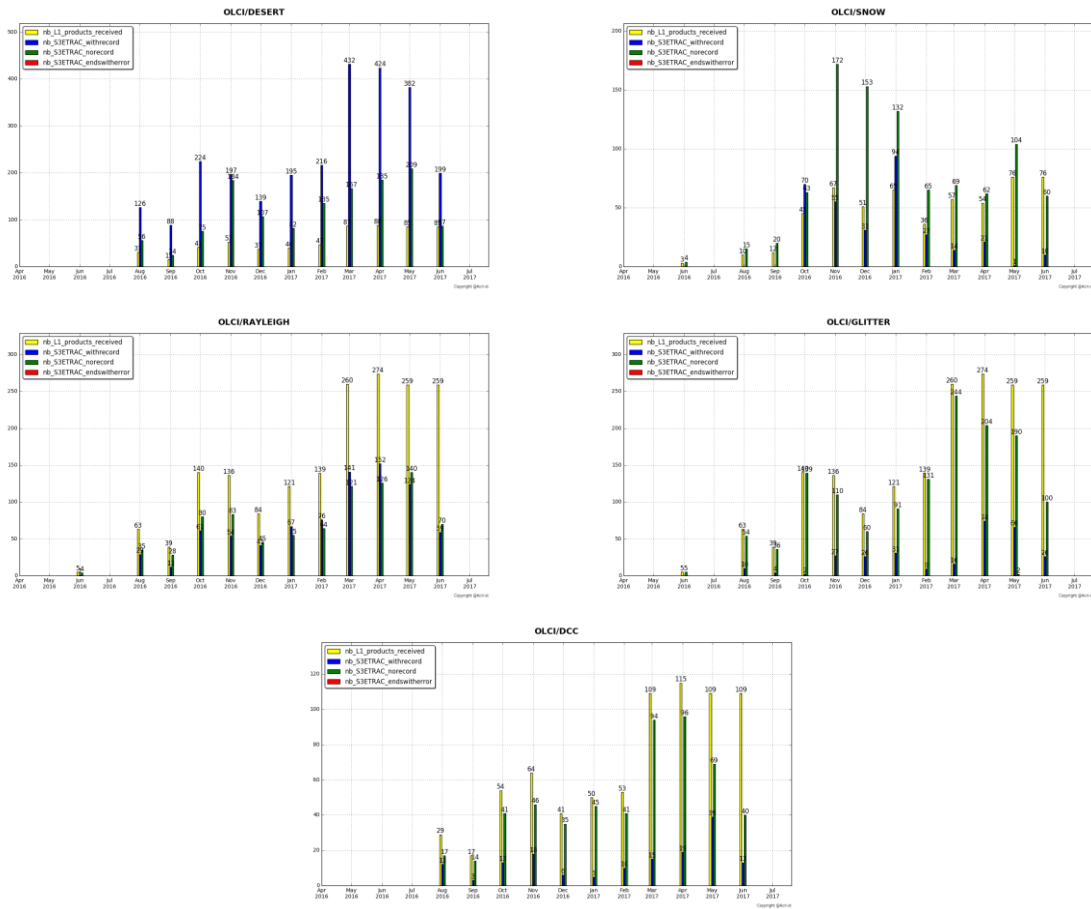


Figure 29: summary of S3ETRAC products generation for OLCI (number of OLCI L1 products Ingested, yellow – number of S3ETRAC extracted products generated, blue – number of S3ETRAC runs without generation of output product (data not meeting selection requirements), green – number of runs ending in error, red, one plot per site type).

2.1.2 Radiometric validation with DIMITRI

Highlights

- Run Rayleigh and Glint methods over the available mini-file (ROIs) until June 15th 2017 from ERR-LN1 products.
- Analysis of OLCI results over Glint, PICS and Rayleigh is performed over the indicated periods (October 2016 – June 2017).
- The results are consistent with the previous results over the three methods, nevertheless, the time-series show higher reflectance over May-June.
- Except Oa01-Oa05 from Rayleigh and Oa17 from Glint, the biases are within the mission requirements (2%); bands with high gaseous absorption are excluded.
- The results are consistent overall the six used PICS sites
- The results need to be consolidated with more products.
- The main issue is the lack of mini-files over DIMITRI-ROIs due to DAPE-issue.



I-Validation over PICS

The ingestion of the l1b time-series over the six desert CalVal sites; from LN1_O_NT products has been extended until 17th June 2017. The whole dataset has been ingested successfully into DIMITRI and automatically (manually when necessary) cloud-screened. Note that only 5 products over the 6 PICS were found during the indicated period, which are not enough to provide a solid analysis. The results are displayed and commented below.

1. The results are consistent overall the six used PICS sites (Figure 30). OLCI reflectance shows strong fluctuation in the beginning of the commissioning phase (about $\pm 8\%$ amplitude) between March and July 2016. Similar fluctuation can be observed over June 2017 leading to probably a strong seasonal signal, but more products over Spring 2017 are needed to confirm this phenomenon.
2. The temporal average over the period **September 2016 – April 2017** of the elementary ratios (observed reflectance to the simulated one) shows values within 2% (mission requirements) over all the VNIR bands (Figure 31). The spectral bands with significant absorption from water vapour and O₂ (Oa11, Oa13 and Oa14) show outlying ratios.

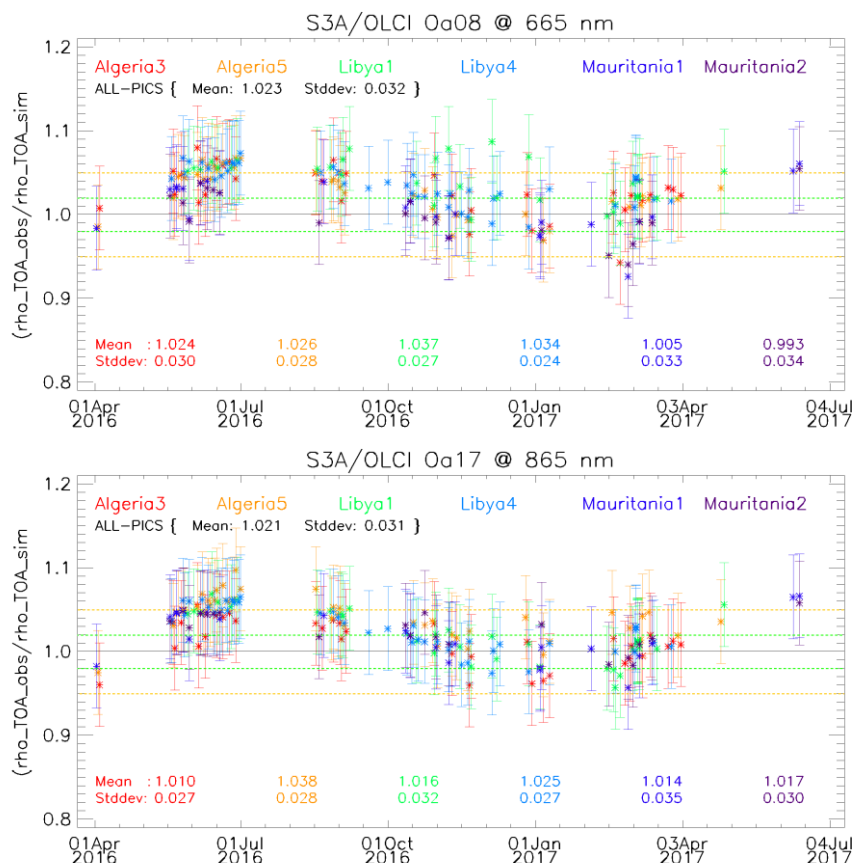


Figure 30: Time-series of the elementary ratios (observed/simulated) signal from S3A/OLCI for (top) band Oa8 and (bottom) band Oa17 over Six PICS Cal/Val sites. Dashed-green and orange lines indicate the 2% and 5% respectively. Error bars indicate the desert methodology uncertainty.

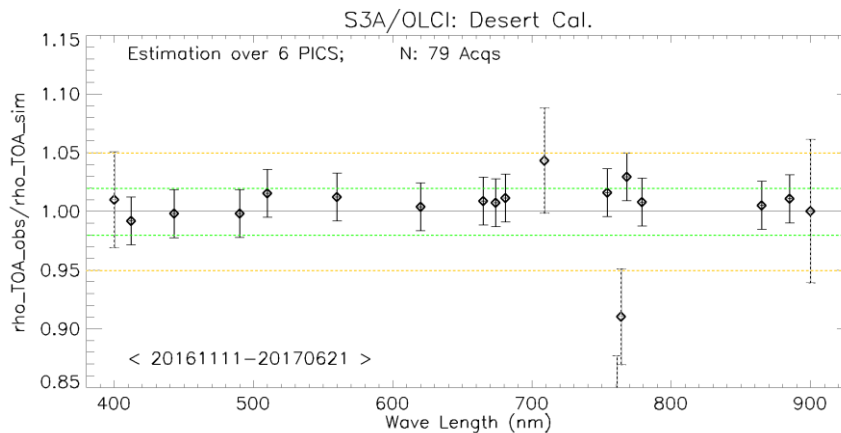


Figure 31: The estimated gain values for S3A/OLCI over the 6 PICS sites identified by CEOS over the period September 2016 – June 2017 as a function of wavelength. Dashed-green and orange lines indicate the 2% and 5% respectively. Error bars indicate the desert methodology uncertainty.

II-Intercomparison S3A/OLCI, S2A/MSI and LANDSAT/OLI over PICS

1. X-mission Intercomparison with MSI-A is done

Figure 32 shows time-series of the elementary ratios from S2A/MSI and S3A/OLCI over Mauritania-1 over the period March-2016 until June-2017.

We observe a clear seasonal fluctuation of OLCI_A ratios which is not the case of MSI_A.

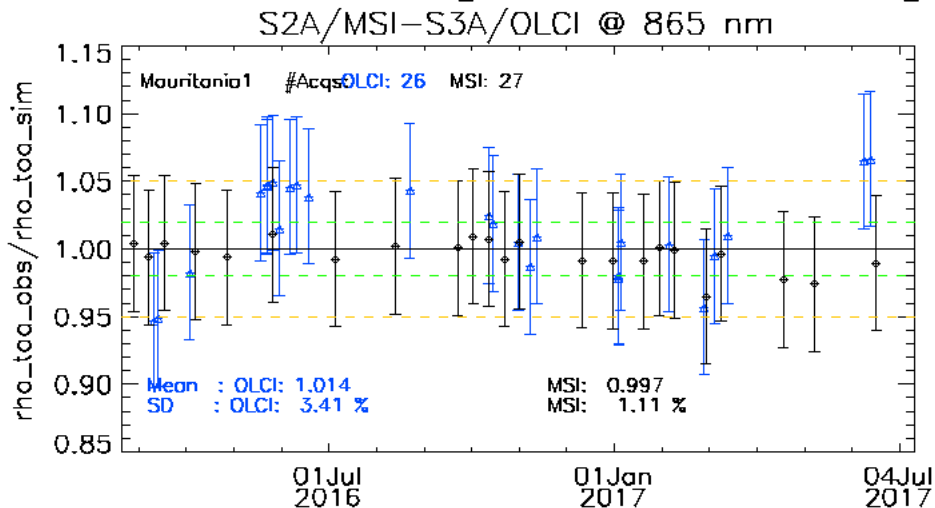


Figure 32: Time-series of the elementary ratios (observed/simulated) signal from (black)S2A/MSI and (blue) S3A/OLCI for band Oa17: 865nm over Mauritania-1 site. Dashed-green and orange lines indicate the 2% and 5% respectively. Error bars indicate the desert methodology uncertainty.

2. We were unable to perform the x-mission Intercomparison with MODIS-A since March 2017 due to an issue with the downloaded L1B-products following to changes on the website (modis.gsfc.nasa.gov).



III-Validation over Rayleigh

Rayleigh method has been run on the CTCP over the available mini-files on the Opt-server. The results produced with the configuration (ROI-AVERAGE) are consistent with the previous results. Note that it has been admitted that DIMITRI gives about 1%-2% higher gain, mainly over bands <500 nm (Figure 33).

IV-Validation over Glint

Glint calibration method with the configuration (ROI-PIXEL) has been performed over the period September 2016 – June 2017 from the available mini-files. The outcome of this analysis shows a good consistency with the desert outputs over the red spectral range (see Figure 33).

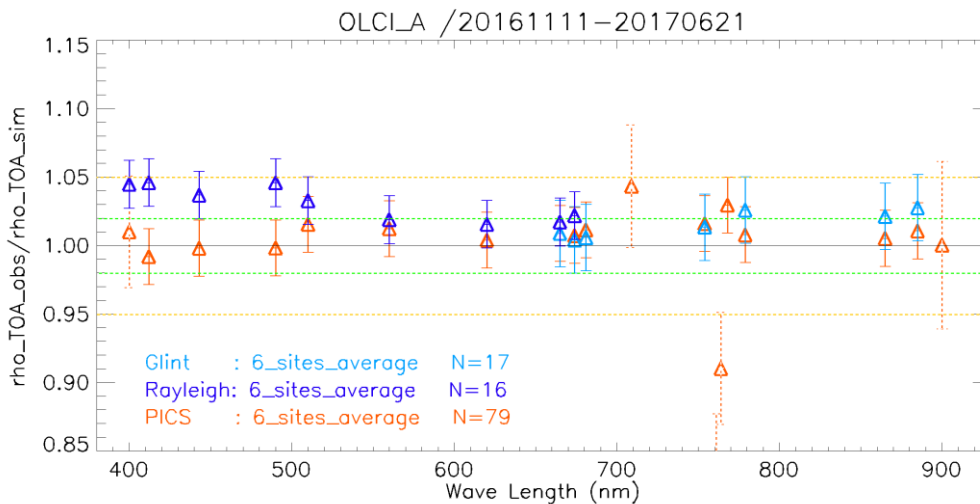


Figure 33: The estimated gain values for S3A/OLCI from Glint, Rayleigh, and PICS over the period November 2016 – June 2017 as a function of wavelength. We use the gain value of Oa8 from Desert method as reference gain for Glint. Dashed-green and orange lines indicate the 2% and 5% respectively. Error bars indicate the methods uncertainties.

2.1.3 Radiometric validation with OSCAR

A preliminary verification of the OLCI radiometry on the basis of the Libya-4 OSCAR desert approach (Govaerts, Y., S. Sterckx, and S. Adriaensen (2013)) has been performed. The approach has been applied to the Libya-4 S3ETRAC acquired in the period March-June 2017. In figure 1 the average results in function of wavelength is given (excluding bands affected by strong oxygen or water vapor absorption). In contrast to the previously reported OSCAR Rayleigh calibration results no strong bias is observed for the first two blue bands.

The OLCI measured values are in average (over all bands) about 3 % larger than the simulated values over the Libya-4 desert sites. However this can be partly explained by the uncertainty in the surface reflectance RPV parameters as small biases (up to 2.8%) were also observed when comparing against



MERIS observations (Govaerts, Y., S. Sterckx, and S. Adriaensen (2013)). Corresponding results are shown on Figure 34.

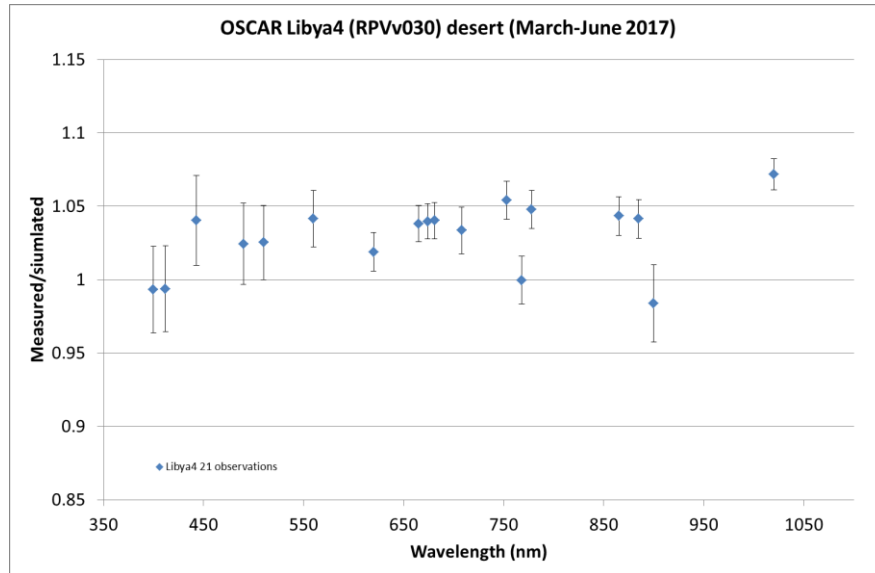


Figure 34: OSCAR Libya-4 deserts results over the period March 2017 –June 2017 in function of wavelength. Only observations with VZA less than 30° are considered. The error bars indicate the standard deviation over the 21 observations.

References

Govaerts, Y., S. Sterckx, and S. Adriaensen (2013). Use of simulated reflectances over bright desert target as an absolute calibration reference. Remote Sensing Letters, , Vol. 4: 6, 523-531.

3 Level 2 Land products validation

3.1 [OLCI-L2LRF-CV-300]

3.1.1 Indirect validation: Temporal evolution of OTCI over core validation sites

11 core validation sites have been selected, incorporating a range of land cover types (Table 2). Data from the core validation sites is expected to be made available through the Sentinel-3 Validation Team (S3VT) during the routine operations phase. However, data availability is not guaranteed during the commissioning phase. Dedicated field campaigns will therefore be required, in which in-situ observations of FAPAR, LAI and Leaf Chlorophyll Concentration (LCC) will be obtained over the core validation sites and upscaled to the spatial resolution of OLCI.

Table 1: Core validation site locations.

Site	Land cover	Latitude	Longitude
DE-Geb	Rainfed cropland	51.1001	10.9143
IT-Cat	Mosaic cropland/vegetation	37.2785	14.8833
IT-Isp	Mosaic vegetation/cropland	45.8128	8.6345
IT-Sro	Closed to open mixed broadleaved and needleleaved forest	43.7278	10.2844
IT-Tra	Mosaic cropland/vegetation	37.6456	12.8666
SP-Ali	Sparse vegetation	38.4516	-1.0646
SP-Val	Rainfed cropland	39.5707	-1.2882
UK-NFo	Mosaic forest or shrubland/grassland	50.8451	-1.5398
US-Ne1	Closed to open herbaceous vegetation	41.1650	-96.4766
US-Ne2	Mosaic cropland/vegetation	41.1648	-96.4701
US-Ne3	Closed to open herbaceous vegetation	41.1797	-96.4396

Mean value of OTCI were calculated over a 3x3 pixels centred around each site using the flowing flags:

INVALID, CLOUD, LAND, SNOW_ICE, COSMETIC, SUSPECT, OTCI_FAIL, OTCI_BAD_IN, OTCI_CLASS_ANG, OTCI_CLASS_CLSN

The figures follow represents temporal evolution for each site for 2016 and 2017. Overall OTCI is tracking the expected temporal pattern of vegetation, and 2017 data are in many cases following a same trajectory as 2016. Most sites show some degree of seasonality except the ITSro site which is an open needle leaved forest. IT-Isp, SP-Val UK-Nfo show the closest match between the 2017 and 2016 OTCI values. Few sites demonstrate winter anomalies further investigation will be undertaken to investigate those.

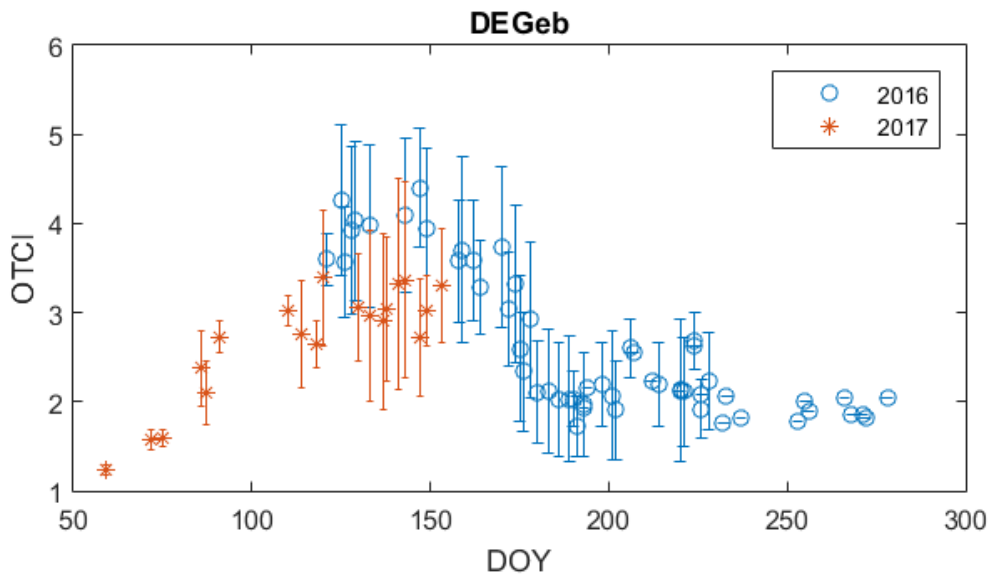


Figure 35: OTCI time series for DEGeb site.

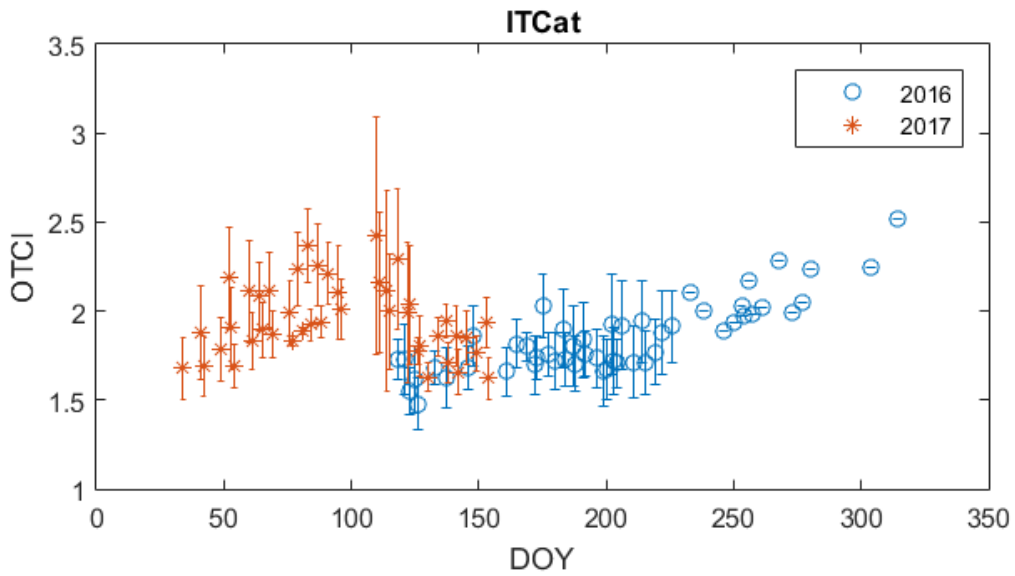


Figure 36: OTCI time series for ITCat site.

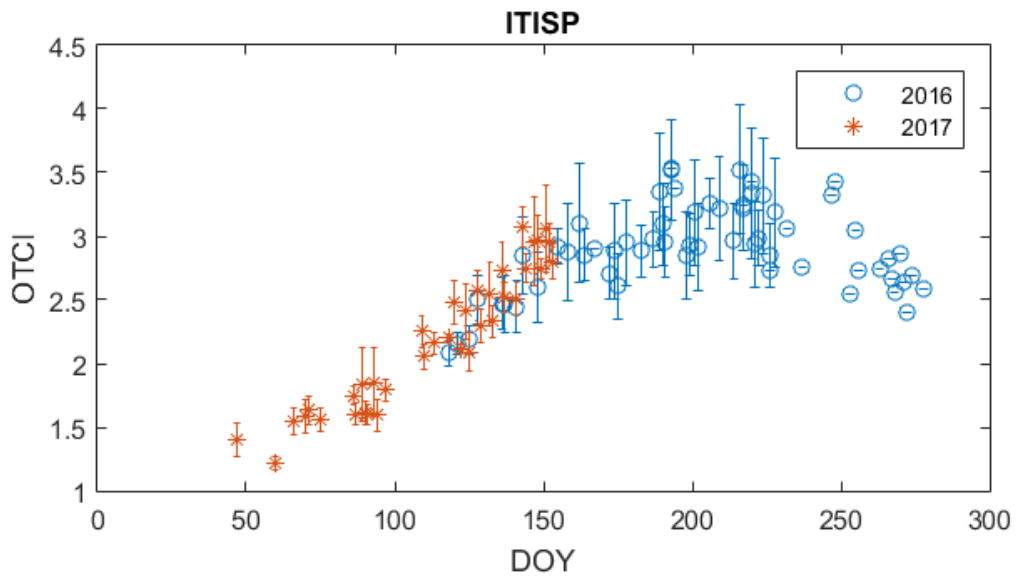


Figure 37: OTCI time series for ITisp site.

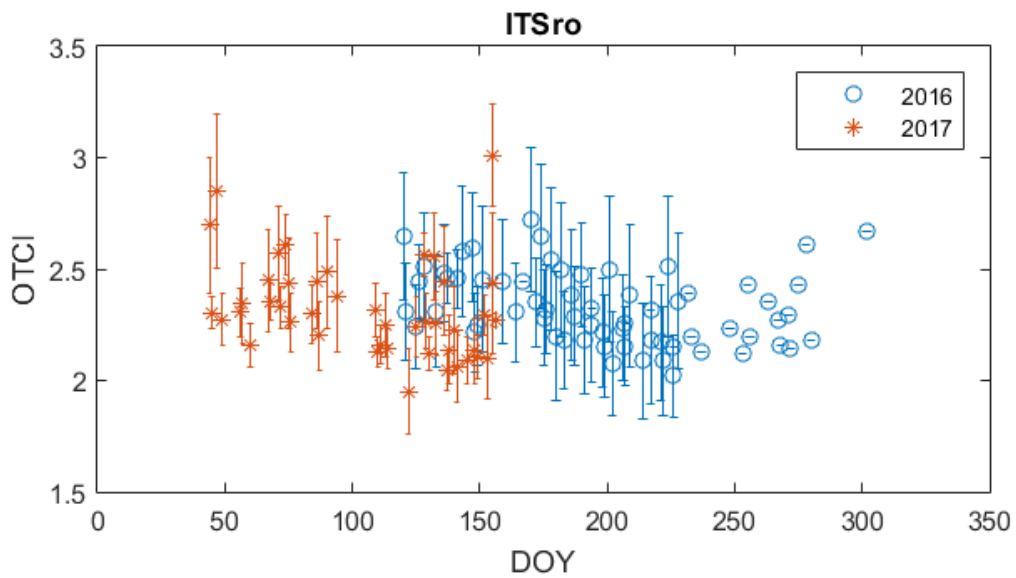


Figure 38: OTCI time series for ITSro site.

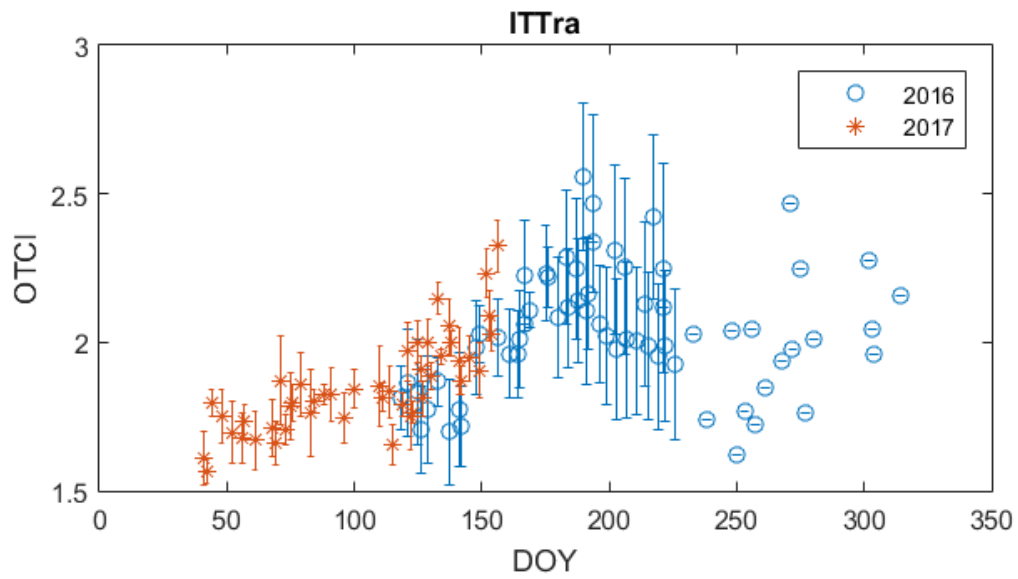


Figure 39: OTCI time series for ITTra site.

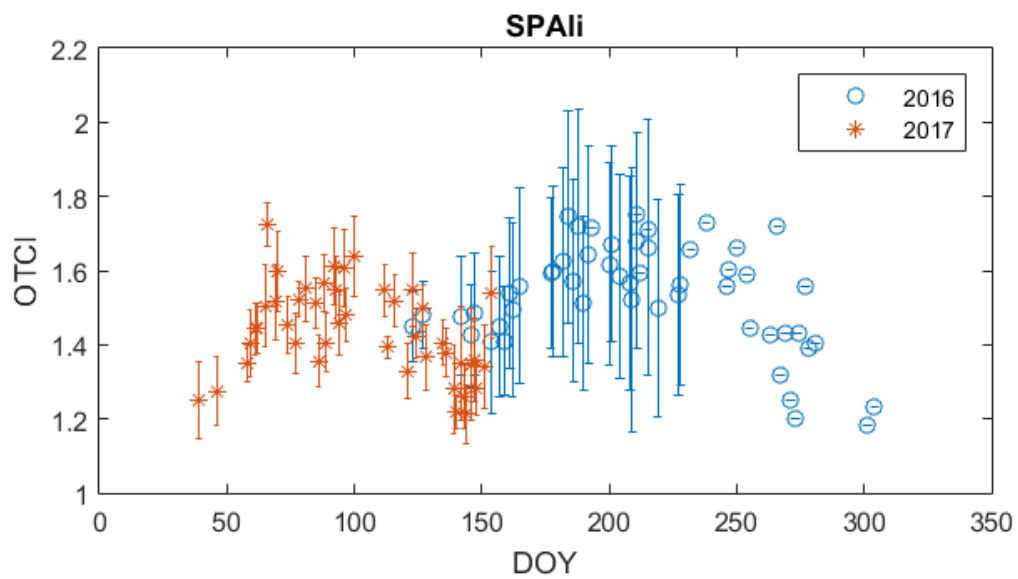


Figure 40: OTCI time series for SPAlI site.

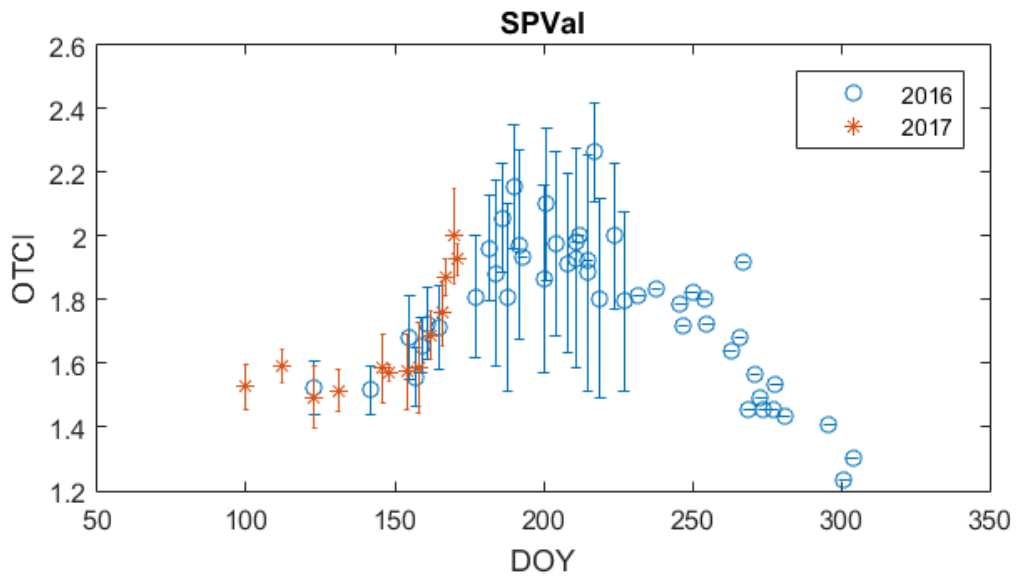


Figure 41: OTCI time series for SPVal site.

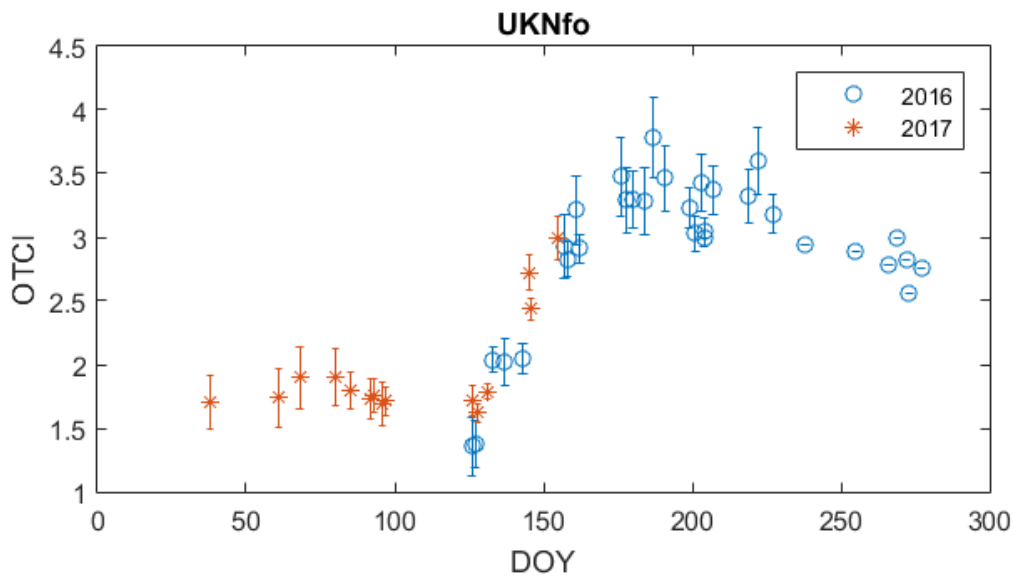


Figure 42: OTCI time series for UKNfo site.

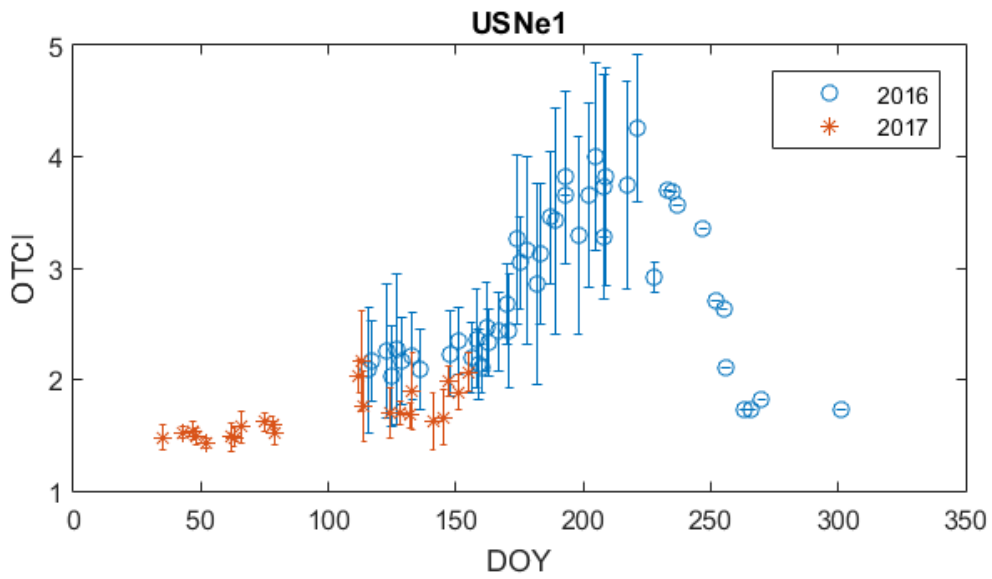


Figure 43: OTCI time series for USNe1 site.

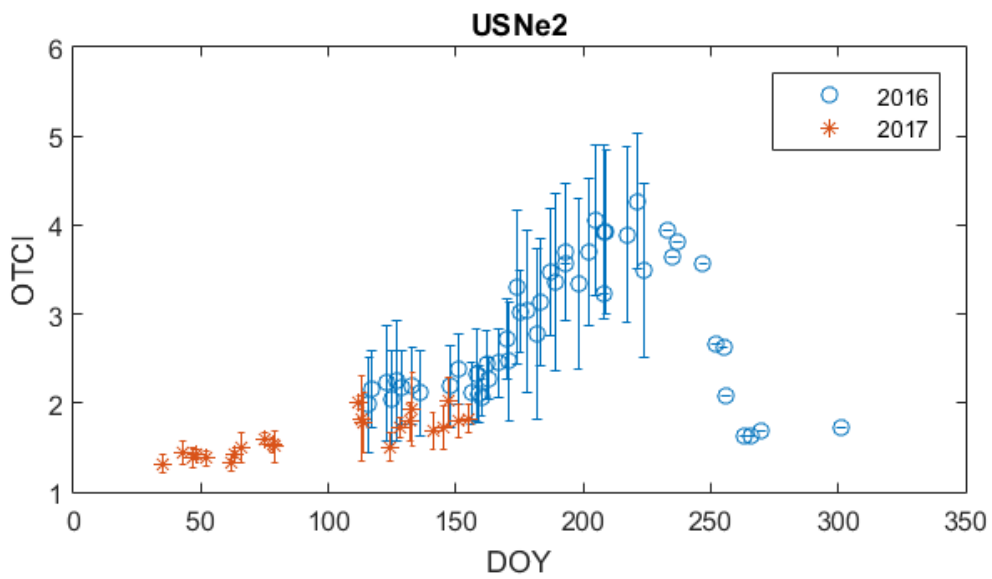


Figure 44: OTCI time series for USNe2 site.

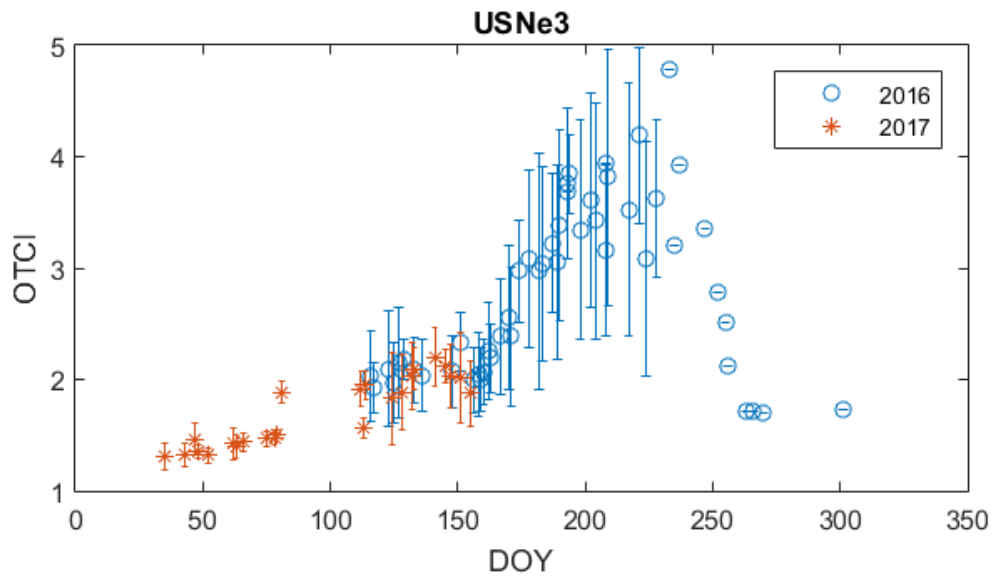


Figure 45: OTCI time series for USNe3 site.

3.1.2 Direct validation: example from UKNfo site

The New Forest site lies approximately 2 km south of Lyndhurst and 3 km north of Brockenhurst in the New Forest, Hampshire, UK. It is comprised of broadleaf deciduous forest with little undergrowth. The dominant species present at the study site are beech (45%), oak (40%) and silver birch (5%), whilst the dominant soil type is a dark grey clay loam.

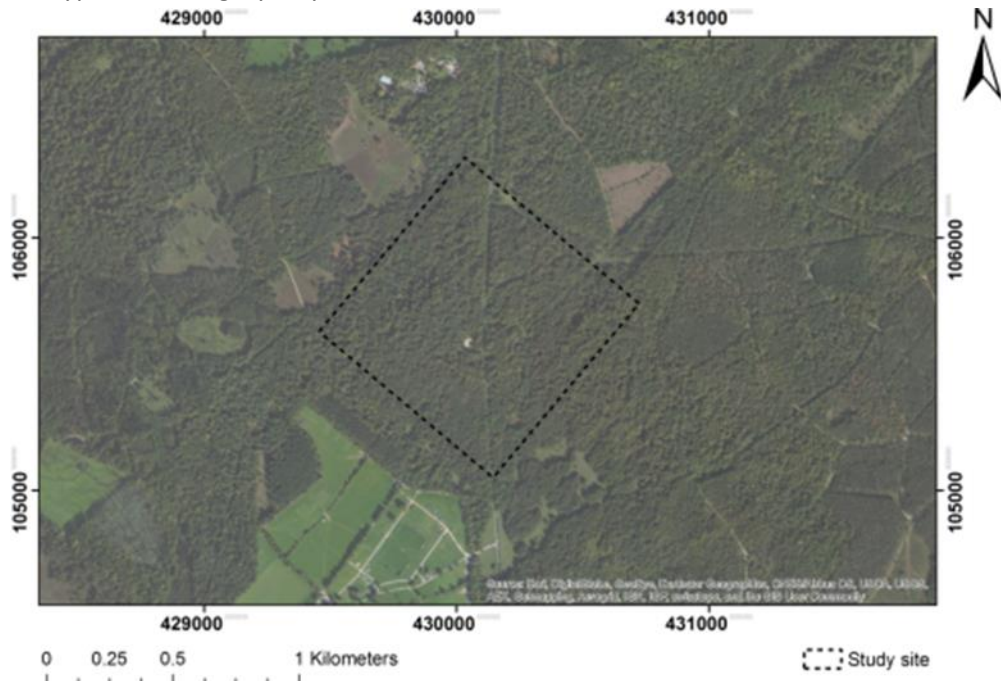


Figure 46: Newforest study site for direct validation.

Measurements of canopy chlorophyll content (CCC) were obtained in 9 elementary sampling units of 40 m x 40 m. Estimates of leaf area index (LAI) were obtained using digital hemispherical photography

(DHP), whilst estimates of leaf chlorophyll concentration (LCC) were obtained using an optical chlorophyll meter. Relative values were converted to absolute LCC using previously published calibration equations. The product of these LAI and LCC variables provided estimates of CCC at the ESU level. Collected in-situ measurements were upscaled to the 300 m spatial resolution of OLCI using Sentinel-2 Multispectral Instrument (MSI) data. Several upscaling options were considered, including the use of the L2B processor incorporated within the Sentinel Applications Platform (SNAP), which uses an artificial neural network (ANN) trained over radiative transfer model (RTM) simulations to retrieve biophysical variables from MSI data. However, a spectral vegetation index similar to the OTCI provided a stronger relationship with in-situ CCC, so an empirical transfer function was adopted. Upscaled maps of CCC were compared with near-contemporaneous OLCI L2 products, after cloud and quality flags were applied. Good performance was demonstrated by a strong linear relationship between the OTCI and upscaled CCC ($R^2 = 0.89$).

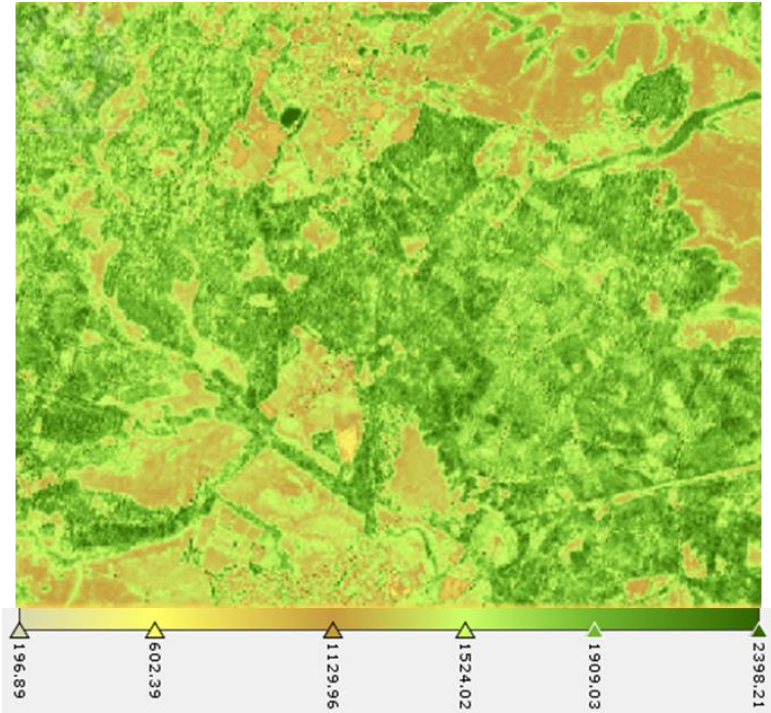


Figure 47: High resolution Canopy chlorophyll content (mg m^{-2}) for the study site.

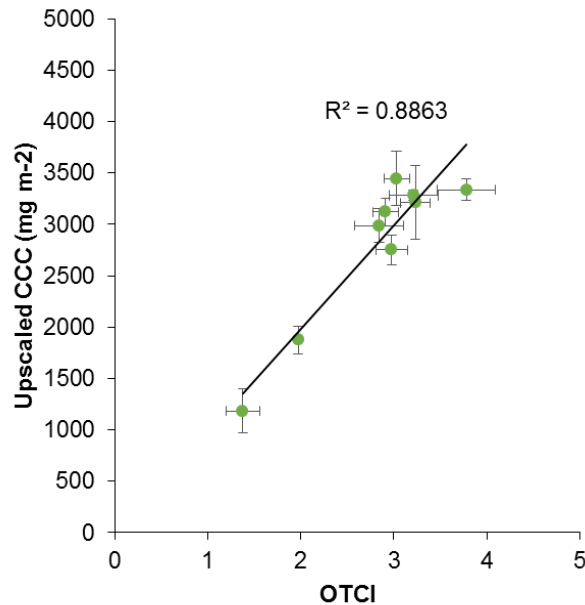


Figure 48: Relationship between canopy chlorophyll content and OTCI over the study site

3.2 [OLCI-L2LRF-CV-410 & OLCI-L2LRF-CV-420] – Cloud Masking & Surface Classification for Land Products

There has been no update on Land Cloud Masking & Surface Classification validation quantitative assessment during the cycle. Last figures (cycle 10) are considered valid.

Qualitative assessment by product inspection showed no detectable performance evolution.

3.3 Validation of Integrated Water Vapour over Land

There has been no update on Integrated Water Vapour over Land validation quantitative assessment during the cycle. Last figures (cycle 15) are considered valid.

Qualitative assessment by product inspection showed no detectable performance evolution.

4 Level 2 Water products validation

4.1 [OLCI-L2-CV-210, OLCI-L2-CV-220] – Vicarious calibration of the NIR and VIS bands

There has been no update on SVC (System Vicarious Calibration) during Cycle 018.

4.2 [OLCI-L2WLR-CV-300, OLCI-L2WLR-CV-310, OLCI-L2WLR-CV-32, OLCI-L2WLR-CV-330, OLCI-L2WLR-CV-340, OLCI-L2WLR-CV-350, OLCI-L2WLR-CV-360 and OLCI-L2WLR-CV-370] – Level 2 Water-leaving Reflectance product validation.

Activities done

- ❖ The focus for this time period has been on the Near Real Time data.
- ❖ All extractions and statistics have been regenerated for the last three months (April 1st 2017 onward; rolling archive limitation). The available matchups therefore cover the spring situation as most of the stations are in the northern hemisphere. Time range available for last processing period covered February 1st to April 30th.
- ❖ MOBY and AERONET-OC in-situ data are available for this time period.

Overall Water-leaving Reflectance performance

Figure 49 below presents the scatter plots with statistics of OLCI versus in situ reflectances computed for the NRT dataset covering the period from April 1st 2016 to June 19th 2017 dataset. As stated in previous reports a positive bias is visible particularly on 412 and 443 nm confirming the need for vicarious calibration. Table 2 below summarises the statistics over the previous period, confirming the important bias at 412 and 443nm. The statistics of the current NRT period are presented in Table 3. Figures remain similar between the two periods.

Table 2: statistics over the previous NRT period (December 2016-March 2017)

lambda	N	RPD	RPD	MAD	RMSE	slope	int.	r2
412	25	70,55%	77,47%	0,0055	0,0071	0,9486	0,0061	0,6787
443	25	43,34%	44,27%	0,0045	0,0056	1,1251	0,0028	0,9037
490	24	28,53%	28,53%	0,0048	0,0059	1,1634	0,0016	0,9611
510	2	31,69%	31,69%	0,0091	0,0093	2,0459	-0,0207	1,0000
560	17	15,44%	16,95%	0,0037	0,0052	1,1350	0,0003	0,9655
665	25	10,56%	34,24%	0,0010	0,0032	1,3661	-0,0013	0,9236

Table 3: statistics over the current NRT period (February 2017-April 2017)

lambda	N	RPD	RPD	MAD	RMSE	slope	int.	r2
412	60	88.15%	93.77%	0.0052	0.0066	1.0404	0.0048	0.6176
443	60	46.70%	50.43%	0.0038	0.0049	1.1195	0.0026	0.8046
490	59	31.38%	32.56%	0.0039	0.0046	1.1397	0.0019	0.9263
510	19	27.06%	27.06%	0.0050	0.0055	1.1474	0.0021	0.9486
560	53	13.42%	16.58%	0.0024	0.0035	1.1281	0.0001	0.9379
665	51	1.02%	29.79%	0.0000	0.0012	1.0202	-0.0001	0.7892



Sentinel-3 MPC

S3-A OLCI Cyclic Performance Report

Cycle No. 018

Ref.: S3MPC.ACR.PR.01-018
 Issue: 1.1
 Date: 22/06/2017
 Page: 41

Table 4 statistics over the current NRT period (April 2017-June 2017)

lambda	N	RPD	RPD	MAD	RMSE	slope	intercept	r2
400	2	17.9%	17.9%	0.0088	0.0100	-2.3992	0.1784	1.0000
412	15	66.3%	66.3%	0.0055	0.0062	1.0618	0.0046	0.9611
443	15	36.7%	37.0%	0.0037	0.0044	1.1107	0.0023	0.9454
490	20	32.1%	32.3%	0.0038	0.0044	1.0153	0.0036	0.8224
510	10	35.9%	35.9%	0.0045	0.0048	0.8626	0.0064	0.7505
560	21	17.0%	21.9%	0.0020	0.0034	1.0925	0.0006	0.9205

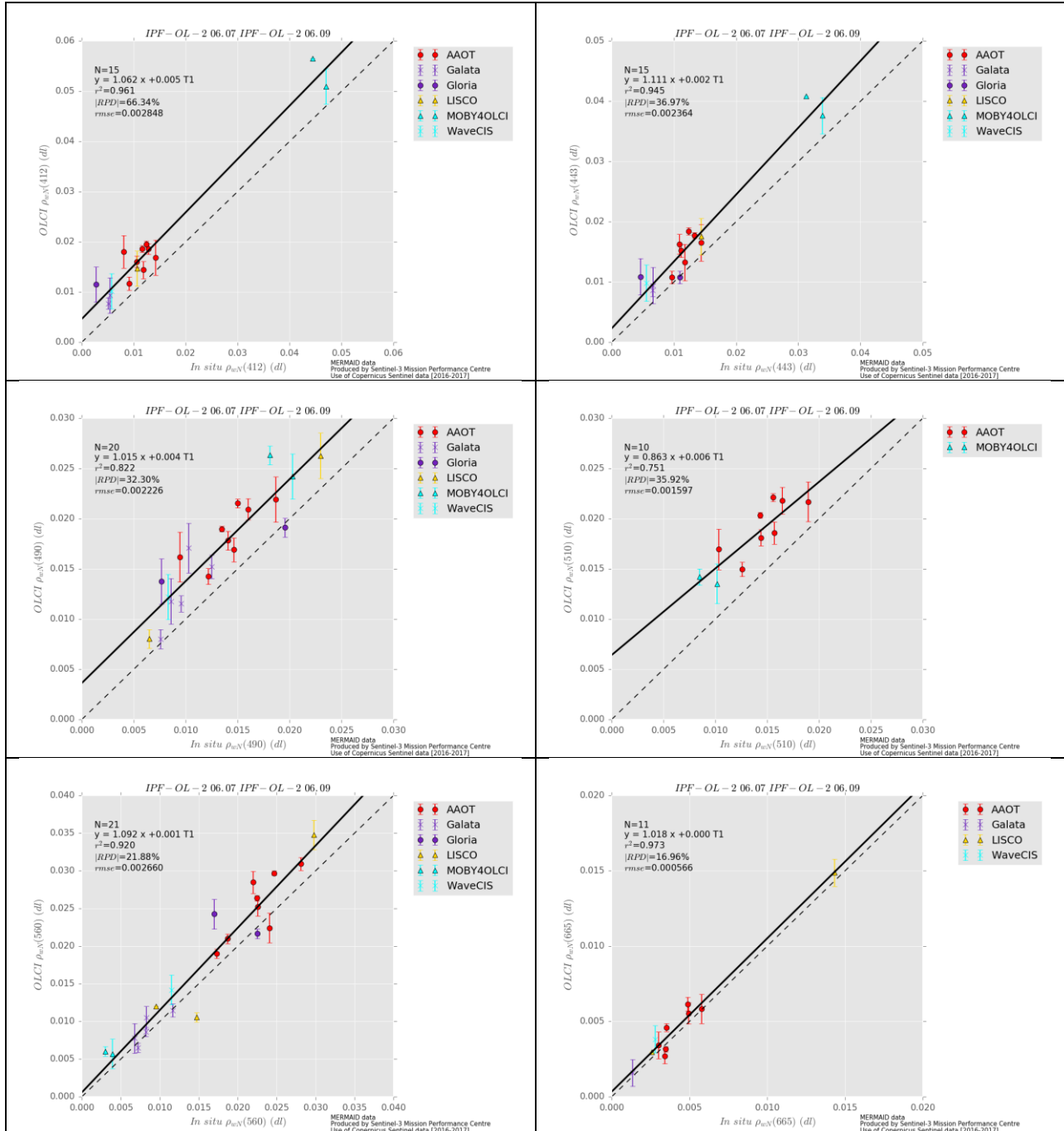


Figure 49: Scatter plots of OLCI versus in situ radiometry

	Sentinel-3 MPC S3-A OLCI Cyclic Performance Report Cycle No. 018	Ref.: S3MPC.ACR.PR.01-018 Issue: 1.1 Date: 22/06/2017 Page: 42
--	---	---

Figure 50 and Figure 51 below show the AAOT and WaveCIS time series derived over the current NRT period. The general cycle on in situ data is well reproduced but these time series confirm the positive bias at 412 and 443nm.



Sentinel-3 MPC

S3-A OLCI Cyclic Performance Report

Cycle No. 018

Ref.: S3MPC.ACR.PR.01-018
Issue: 1.1
Date: 22/06/2017
Page: 43

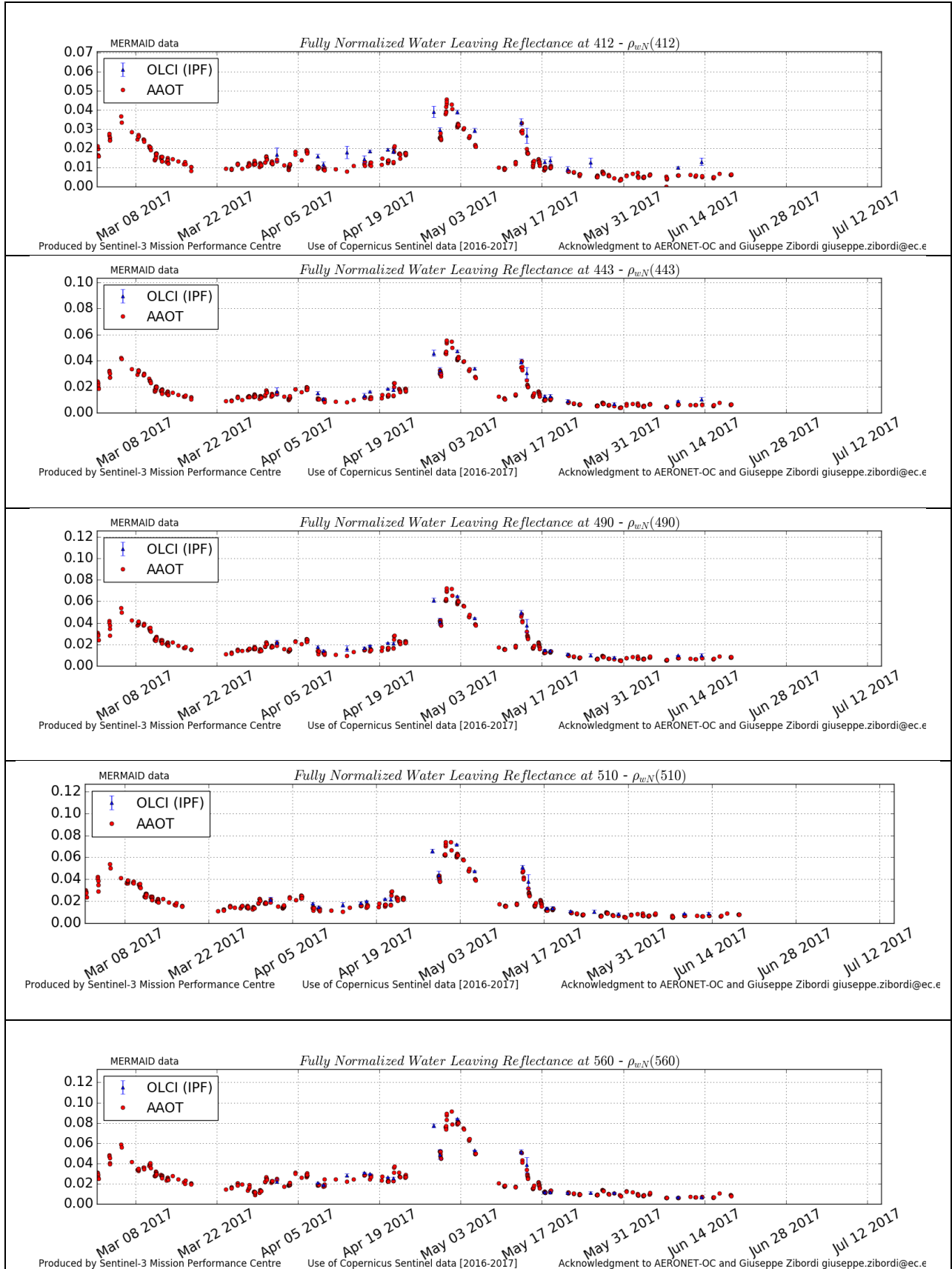


Figure 50: OLCI and AERONET-OC radiometric time series AAOT station.



Sentinel-3 MPC
S3-A OLCI Cyclic Performance Report
Cycle No. 018

Ref.: S3MPC.ACR.PR.01-018
 Issue: 1.1
 Date: 22/06/2017
 Page: 44

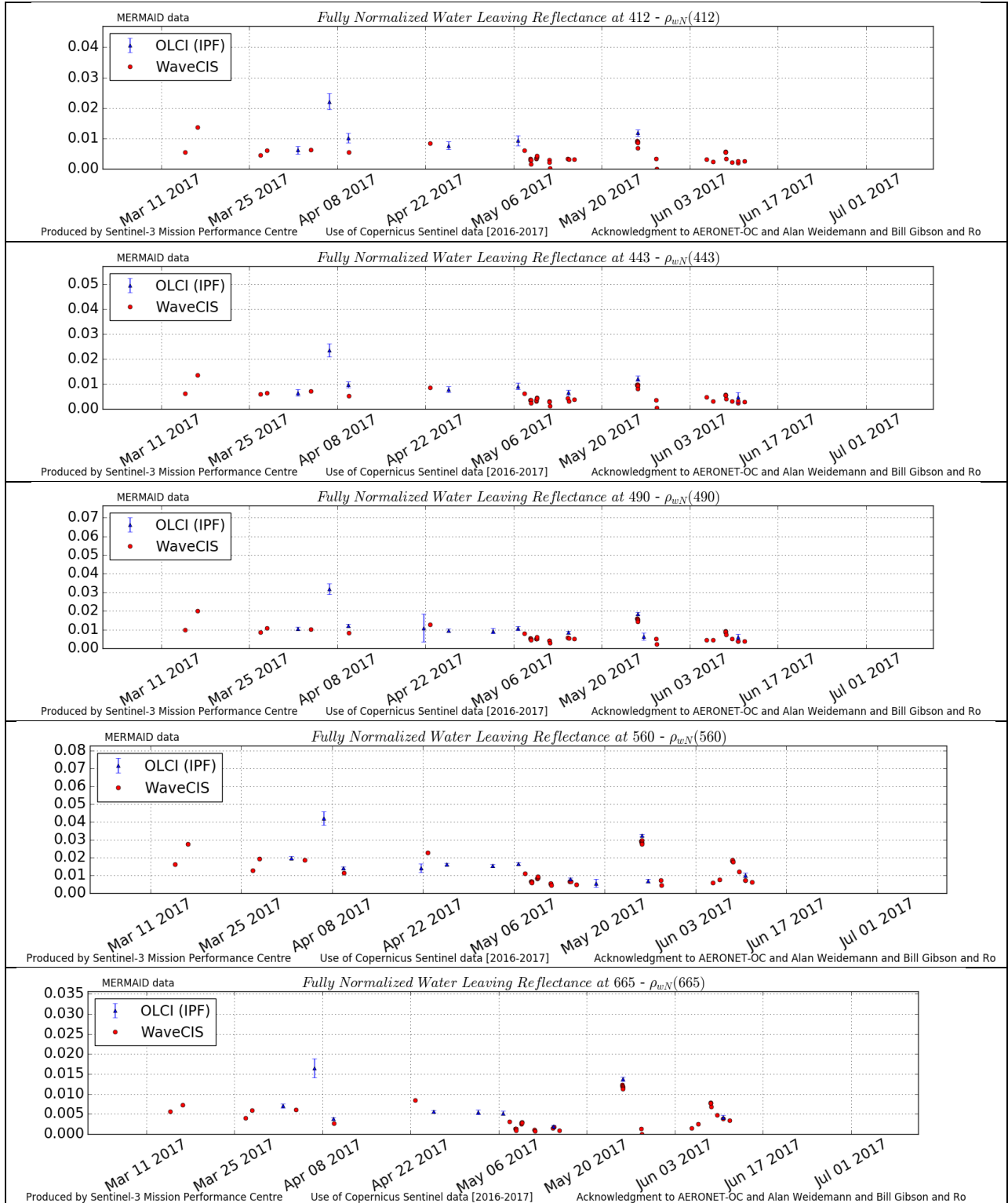


Figure 51: OLCI and AERONET-OC radiometric time series Wave-CIS station.

	<p>Sentinel-3 MPC</p> <p>S3-A OLCI Cyclic Performance Report</p> <p>Cycle No. 018</p>	<p>Ref.: S3MPC.ACR.PR.01-018</p> <p>Issue: 1.1</p> <p>Date: 22/06/2017</p> <p>Page: 45</p>
--	--	--

4.3 [OLCI-L2WLR-CV530] Validation of Aerosol Product

Summary of activities

The aerosol properties, estimated within the atmospheric correction process, are consistent with expectations taken from former AERONET products. In cloud and sun-glint contaminated areas the aerosol optical thickness is retrieved unrealistically high, however, the estimated chlorophyll concentration seems to be often nearly unaffected.

Activities done

A verification of the product quality has been performed for numerous scenes, mainly in the tropical Pacific and Atlantic Ocean.

In general, the range of aerosol optical thickness (T865) and the Angstrom coefficient (A865) values are consistent with the expectation of low values for T865 (<0.1) and A865 (0.2-1.8) above clear open ocean atmospheres, when no cloud contamination and/or sun-glint is present.

But we found a significant number of pixels with unrealistic high T865 values (up to 0.8), which often correlate with low Ångstrom coefficients. Particularly in areas where different cloud types occur, small undetected cumulus or cirrus clouds. This results in not realistic T865 and A865 retrievals above open oceans.

We investigated several orbits of the S3 L2 products: IWV, T865, A865, but also chl_OC4ME to understand how the atmospheric correction and possible errors transfer into the ocean product.

Figure 52 shows a profile of the aerosol optical thickness T865 in the middle of the Pacific (9°37' N, 176° E), part of the OLCI scene from 15.03.2017 (21:43.45-22:27.42). The high and medium glint area is marked in turquoise and green. The lower values of T865 are around 0.1, but there are high variations with values higher than 0.5, which are too large for this open ocean area. This is very likely due to cloud contamination, by small cumulus or by insufficient corrected white caps. Towards the medium and high glint area T865 is steadily increased to values up to 0.8. This clearly indicates, that T865 is not correctly estimated above glint areas. The variability of T865 is even higher when the entire area, as shown in Figure 52, is analyzed.

The Ångström coefficient varies between 0.25 and 1.7, even within short distances (see Figure 53). Towards the glint A865 is drastically increasing. All this is not realistic and would lead to misinterpretations of the aerosol optical properties and causes for their dynamics.

The derived chlorophyll product is surprisingly unaffected to the unrealistically derived aerosol products, but there are spikes and areas of high chlorophyll concentrations, which has to be verified by a thorough analysis (see Figure 52 and Figure 53).

The integrated water vapour IWV-product is within the expected range, but the variability has to be studied with respect to cloud contamination (see Figure 52 and Figure 53).

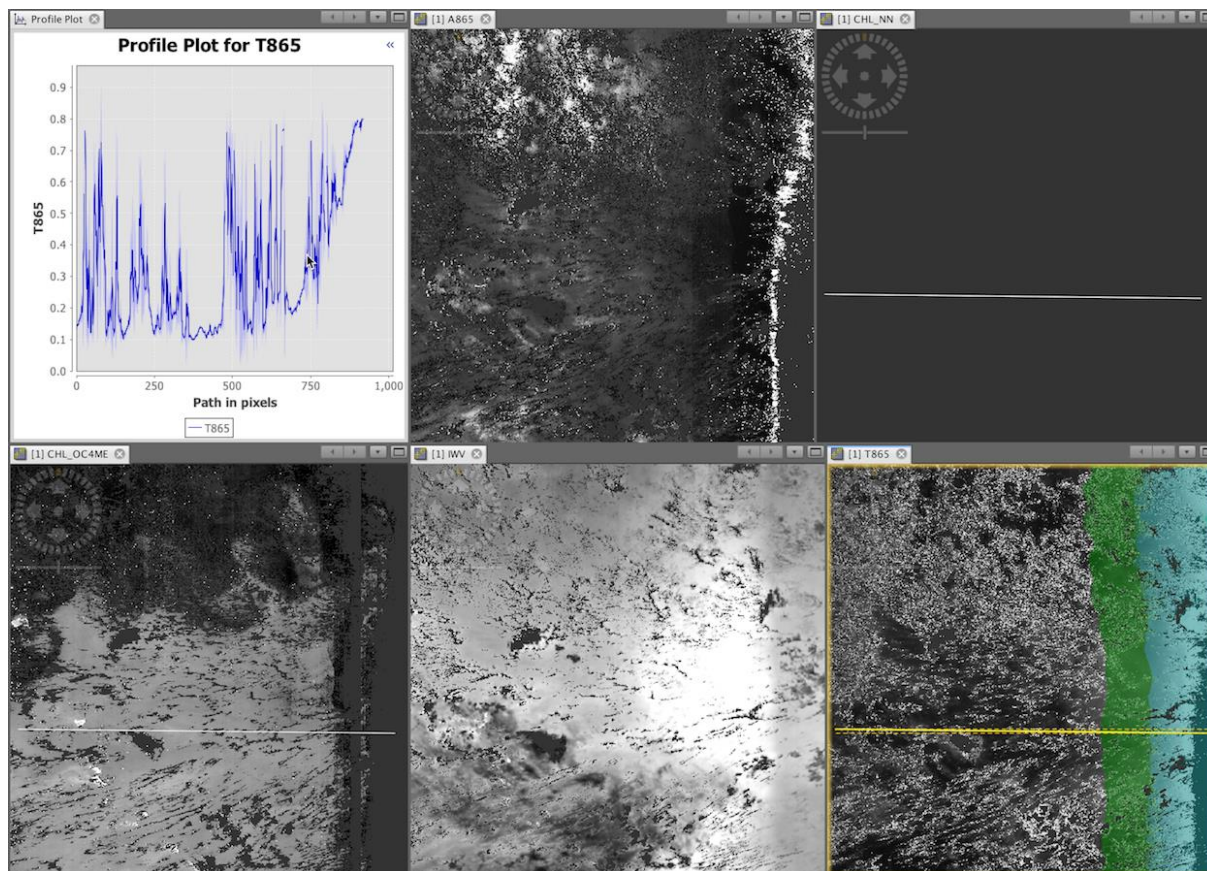


Figure 52: Profile of aerosol optical thickness T865 (upper left), an image of T865 with the yellow line for which T865 is retrieved (lower right), Ångström coefficient A865 (upper middle), OC4ME (lower left) and IWV (lower middle); the OLCI scene from 15.03.2017 (21:43.45-22:27.42) is at 9°37' N and 176° E.

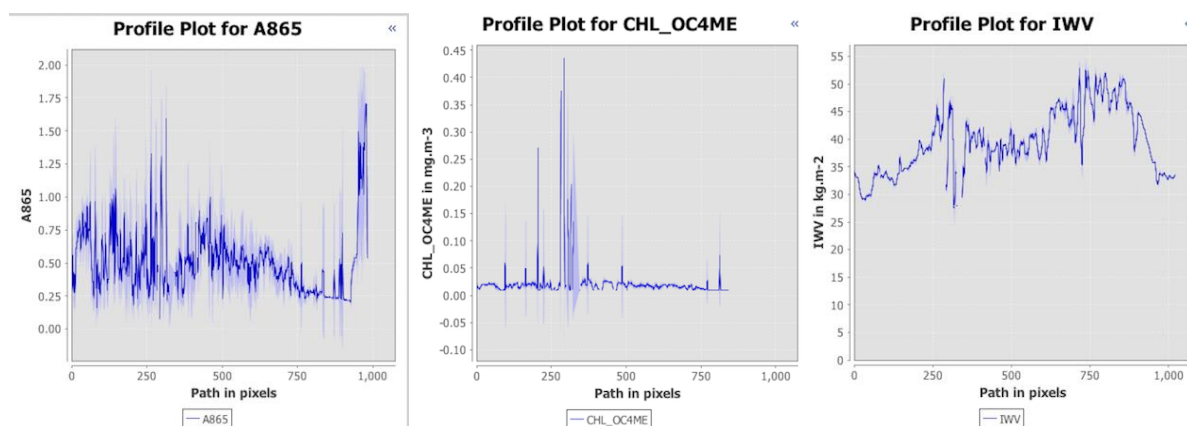


Figure 53: Profile of Ångström coefficient A865 (left), of CHL_OC4ME (middle), and of IWV (right), see Figure 52 for further details.

To understand the high variability of the aerosol properties T865 and A865 better, we made a close up in the same region (see Figure 54). The profile plot of T865 shows values of 0.05, which is realistic for this region, well known for one of the cleanest air conditions on our globe. The selected area shows a very high number of scattered large T865 values. The lower and more realistic T865 is, the smoother the

A865 field is. Within this area a derived Ångström coefficient A865 of about 0.8 indicates the presence of maritime aerosols (Toledano et al, 2007). The IWV seems to be less affected and is quite homogeneously distributed within the considered area. Nevertheless, the observed variations can be caused by a change of dark and white caps impacted pixels or sub-pixel clouds (see Figure 54 and Figure 55). Nevertheless, there are sampling effects around cloud areas. We suspect that pixels are sampled which are in the vicinity of detected clouds. We recommend not using those pixels by excluding not only cloudy pixels but also pixels in the vicinity of clouds, eg. minimum distance of 4 RR-pixels.

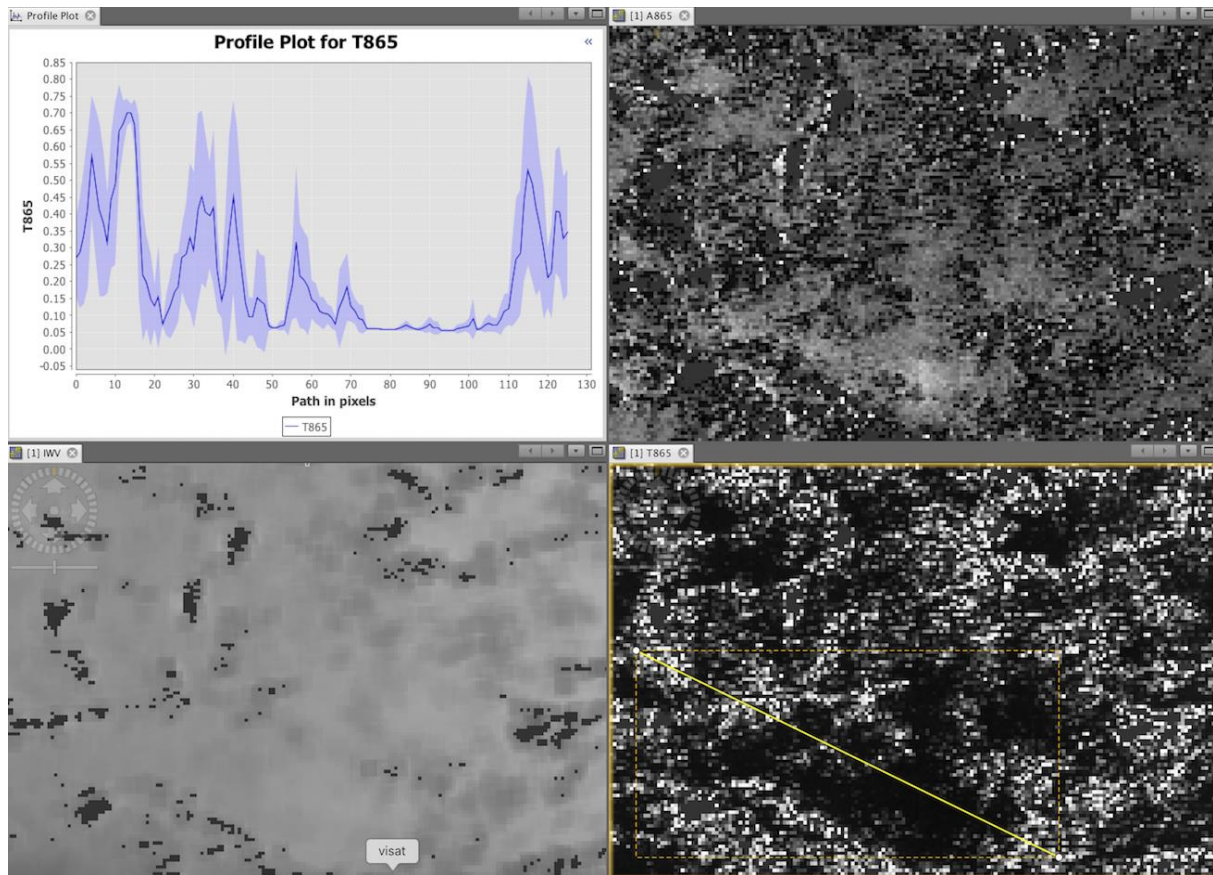


Figure 54 Profile of aerosol optical thickness T865 (upper left), an image of T865 with the yellow line for which T865 is retrieved (lower right), Ångström coefficient A865 (upper right), and IWV (lower left); OLCI scene at 15°36' N and 178° E from 15.03.2017 (21:43.45-22:27.42).

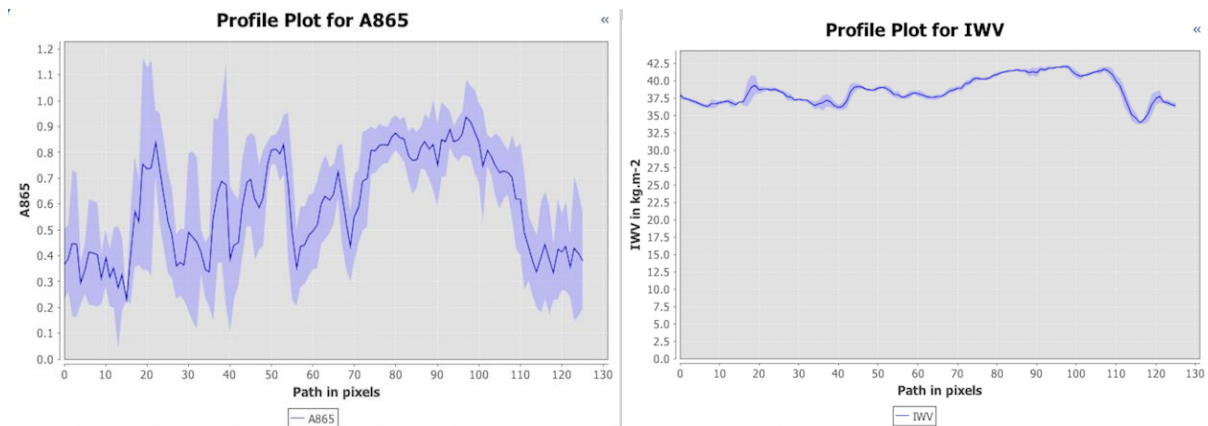


Figure 55: Profile of Ångström coefficient A865 (left) and of IWV (right), see Figure 54 for further details.

A profile along close to the equator of T865 shows high values, which are very likely related to cloud contamination and/or sun-glint and white caps (Figure 56). The red arrow points to the pixel for which the reflectance spectrum is shown as well in Figure 56. The reflectance value at 778 nm is unrealistically high within the entire spectrum and cannot be explained by means of radiative transfer.

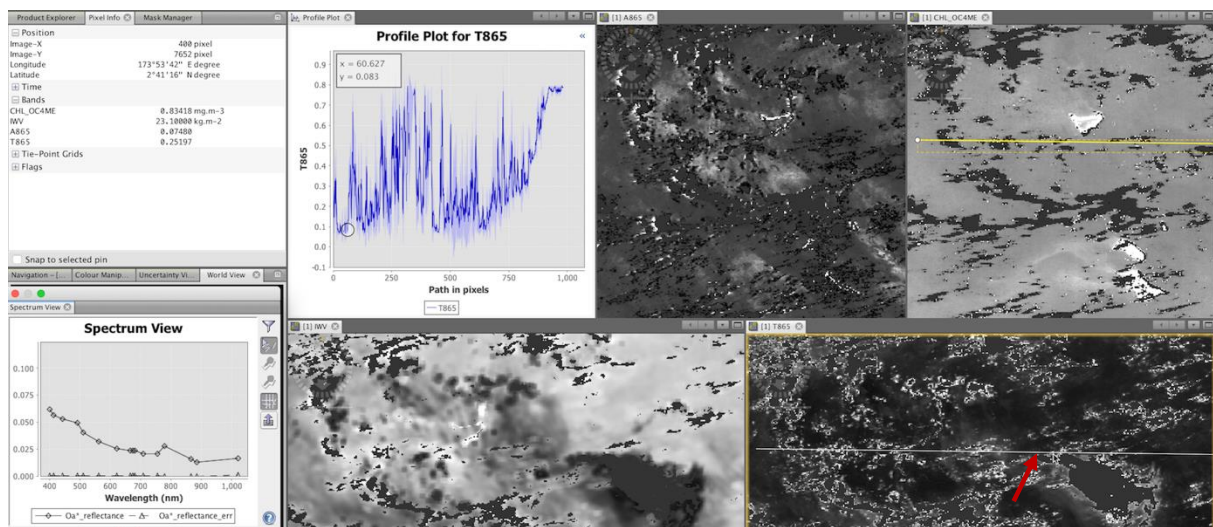


Figure 56: Profile of aerosol optical thickness T865 (upper left), an image of T865 with the line for which T865 is retrieved (lower right) and the red arrow, pointing to the pixel for which the reflectance spectrum is displayed (lower left), Ångström coefficient A865 (upper middle), OC4ME (upper right) and IWV (lower middle); the OLCI scene from 15.03.2017 (21:43.45-22:27.42) is at 2°41' N and 173°54' E.

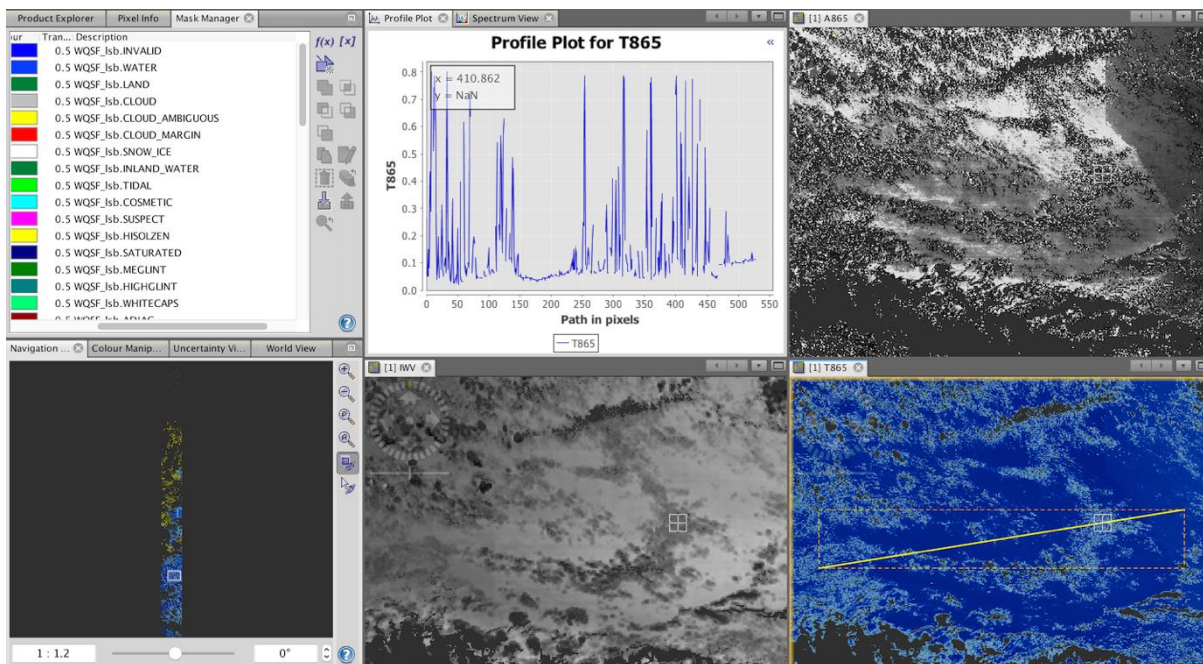


Figure 57: Profile of aerosol optical thickness T865 (upper middle), an image of T865 with the yellow line for which T865 is retrieved (lower right), Ångström coefficient A865 (upper right), and IWV (lower middle), the cloud flag is set (yellow); OLCI scene at 16° S and 102° E from 10.05.2017 (02:14.42-02:59.04).

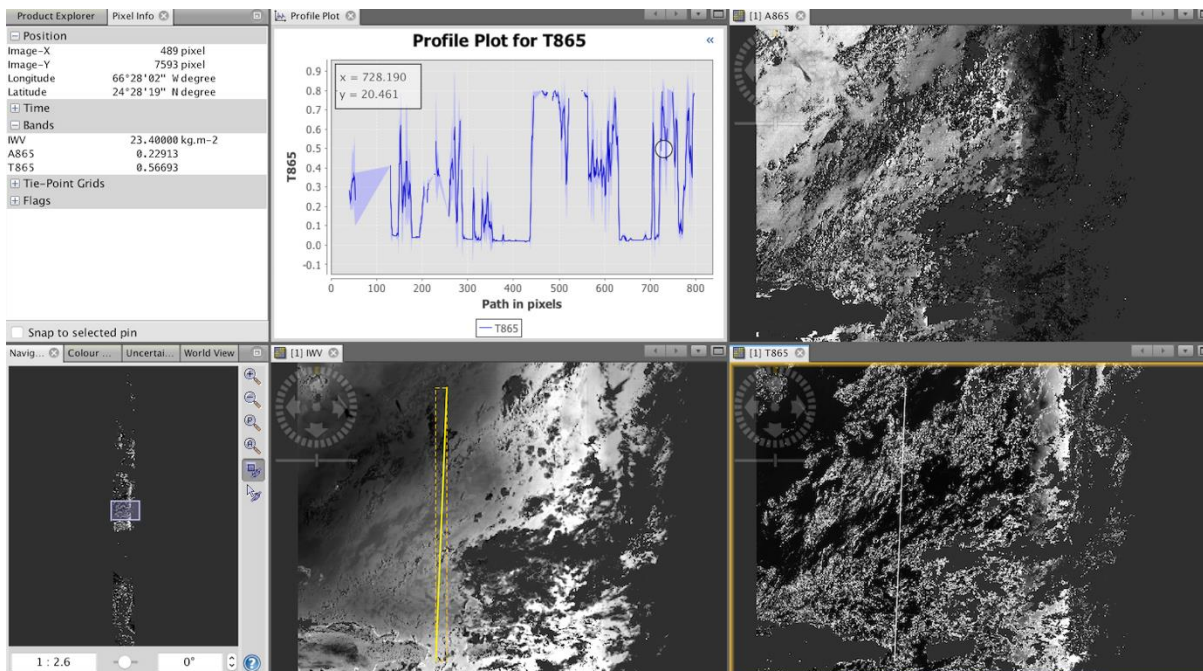


Figure 58: Profile of aerosol optical thickness T865 (upper middle), an image of T865 with the line for which T865 is retrieved (lower right), Ångström coefficient A865 (upper right), and IWV (lower middle); OLCI scene at 24° S and 66° W from 10.05.2017 (14:01.34-14:45.57).

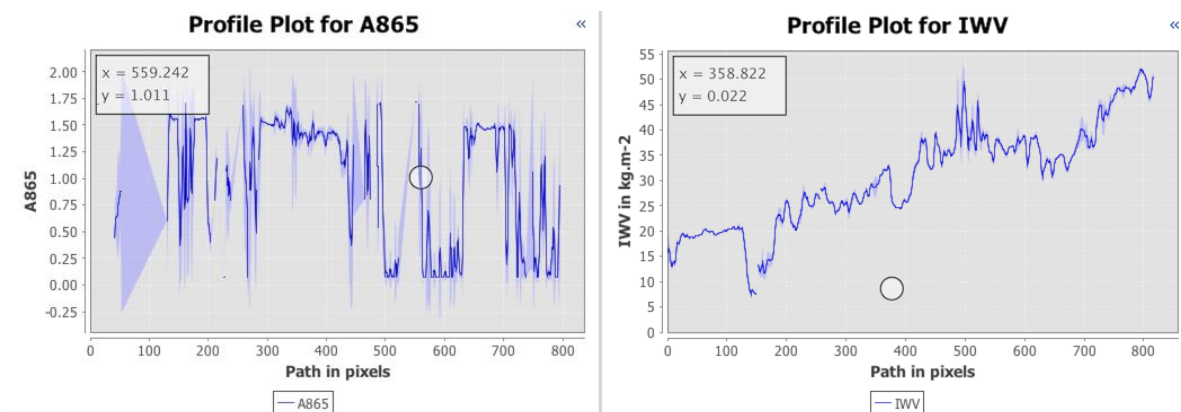


Figure 59: Profile of T865 (left) and IWV (right); OLCI scene at 24° S and 66° W from 10.05.2017 (14:01.34-14:45.57), see Figure 58.

To summarize the findings of these investigations we state:

- In general, the aerosol optical thickness T865 and the Ångström coefficient A865 are derived within the expected range; there are reasonable and realistic, when derived under perfect conditions.
- There are a significant and not tolerable number of pixels, for which T865 and A865 are not realistic and
- We postulate that the retrieval of T865 and A865 is affected by
 - cloud contamination and cloud shadow
 - white caps
 - sun glint
- T865 is derived in glint, but unrealistically high; T865 and A865 retrieval above glint has to be significantly improved, even when CHL is not derived, but the aerosol properties are used in atmospheric chemistry and climate studies.
- There are more derived IWV pixels then for T865, but both should be retrieved only under clear conditions. Why? Is this related to a non-converging aerosol retrieval?
- The L2 reflectance (Oa*) spectrum close to clouds is sometimes unrealistic (see Figure 56 lower left) for unknown reasons. The values are far from saturation.
- O2A bands and WV-bands are good indicators for clouds: use at least all the OLCI channels for cloud masking: full spectrum plus aerial information!

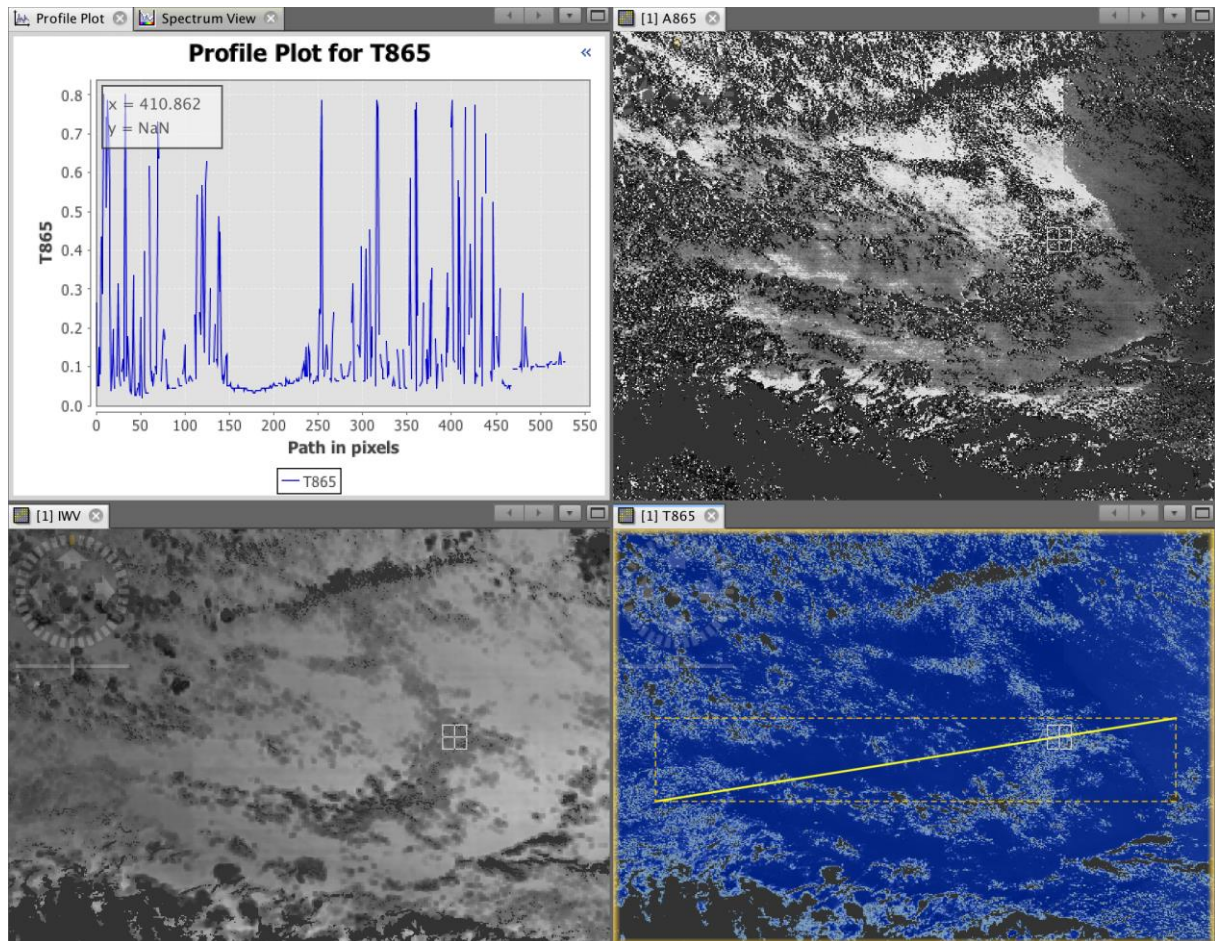


Figure 60: Profile of aerosol optical thickness T865 (upper left), an image of T865 with the yellow line for which T865 is retrieved (lower right), Ångström coefficient A865 (upper right), and IWV (lower middle); OLCI scene from 10.05.2017 (14:01.34-14:45.57).

Next steps

- In general: a validation of the aerosol products by Aeronet sites is critical, because the main problems arise under glint and cloud contamination.
- A thorough investigation, considering L1 and L2 products (FR and RR), has to be performed:
 - e.g. correlate aerosol products with cloud properties (problematic, since S3 has no CTP product) and distance from clouds;
 - consider also different measuring conditions, defined by Met-dat (e.g. wind speed → white caps)
- We are collecting Aeronet data for specific locations, to perform a quantitative validation for situations, where the before mentioned problems might not arise.

	Sentinel-3 MPC S3-A OLCI Cyclic Performance Report Cycle No. 018	Ref.: S3MPC.ACR.PR.01-018 Issue: 1.1 Date: 22/06/2017 Page: 52
--	---	---

5 Level 2 SYN products validation

5.1 [SYN-L2-CV-100]

There has been no update on SYN products validation quantitative assessment during the cycle. Last figures (cycle 10) are considered valid.

Qualitative assessment by product inspection showed no detectable performance evolution.

 <p>SENTINEL 3 Mission Performance Centre</p>	<p>Sentinel-3 MPC</p> <p>S3-A OLCI Cyclic Performance Report</p> <p>Cycle No. 018</p>	<p>Ref.: S3MPC.ACR.PR.01-018</p> <p>Issue: 1.1</p> <p>Date: 22/06/2017</p> <p>Page: 53</p>
---	--	--

6 Events

One OLCI Radiometric Calibration Sequence has been acquired during Cycle 018:

- ❖ S01 sequence on 28/05/2017 20:35 to 20:37 (absolute orbit 6653)

	Sentinel-3 MPC S3-A OLCI Cyclic Performance Report Cycle No. 018	Ref.: S3MPC.ACR.PR.01-018 Issue: 1.1 Date: 22/06/2017 Page: 54
--	---	---

7 Appendix A

Other reports related to the Optical mission are:

- ❖ S3-A SLSTR Cyclic Performance Report, Cycle No. 018 (ref. S3MPC.RAL.PR.02-018)

All Cyclic Performance Reports are available on MPC pages in Sentinel Online website, at:
<https://sentinel.esa.int>

End of document